Monthly Notices
of the
ROYAL ASTRONOMICAL SOCIETY

MNRAS **472,** 2651–2669 (2017)
Advance Access publication 2017 August 19

doi:10.1093/mnras/stx2118

Simultaneously constraining the astrophysics of reionization and the epoch of heating with 21CMMC

Bradley Greig★ and Andrei Mesinger
Scuola Normale Superiore, Piazza dei Cavalieri 7, I-56126 Pisa, Italy

Accepted 2017 August 11. Received 2017 August 10; in original form 2017 May 9

ABSTRACT

The cosmic 21 cm signal is set to revolutionize our understanding of the early Universe, allowing us to probe the 3D temperature and ionization structure of the intergalactic medium (IGM). It will open a window on to the unseen first galaxies, showing us how their UV and X-ray photons drove the cosmic milestones of the epoch of reionization (EoR) and epoch of heating (EoH). To facilitate parameter inference from the 21 cm signal, we previously developed 21CMMC: a Monte Carlo Markov Chain sampler of 3D EoR simulations. Here, we extend 21CMMC to include simultaneous modelling of the EoH, resulting in a complete Bayesian inference framework for the astrophysics dominating the observable epochs of the cosmic 21 cm signal. We demonstrate that second-generation interferometers, the Hydrogen Epoch of Reionization Array and Square Kilometre Array will be able to constrain ionizing and X-ray source properties of the first galaxies with a fractional precision of the order of $\sim$1–10 per cent (1σ). The ionization history of the Universe can be constrained to within a few percent. Using our extended framework, we quantify the bias in EoR parameter recovery incurred by the common simplification of a saturated spin temperature in the IGM. Depending on the extent of overlap between the EoR and the EoH, the recovered astrophysical parameters can be biased by $\sim 3\sigma$–10σ.

Key words: galaxies: high-redshift – intergalactic medium – dark ages, reionization, first stars – diffuse radiation – early Universe – cosmology: theory.

1 INTRODUCTION

The 21 cm spin-flip transition of neutral hydrogen encodes a treasure trove of cosmological and astrophysical information (see e.g. Gnedin & Ostriker 1997; Madau, Meiksin & Rees 1997; Shaver et al. 1999; Tozzi, Madau, Meiksin & Rees 2000; Gnedin & Shaver 2004; Furlanetto, Oh & Briggs 2006; Morales & Wyithe 2010; Pritchard & Loeb 2012). The signal is expressed as the offset of the 21 cm brightness temperature, $\delta T_{\rm b}(\nu)$, relative to the cosmic microwave background (CMB) temperature, $T_{\rm CMB}$ (e.g. Furlanetto et al. 2006):

$$\delta T_{\rm b}(\nu) \approx 27 x_{\rm H\,I}(1+\delta_{\rm nl}) \left(\frac{H}{{\rm d}v_{\rm r}/{\rm d}r + H}\right) \left(1 - \frac{T_{\rm CMB}}{T_{\rm S}}\right) \times \left(\frac{1+z}{10}\frac{0.15}{\Omega_{\rm m}h^2}\right)^{1/2} \left(\frac{\Omega_{\rm b}h^2}{0.023}\right) {\rm mK}, \quad (1)$$

where $x_{\rm H\,I}$ is the neutral fraction, $T_{\rm S}$ is the gas spin temperature, $\delta_{\rm nl} \equiv \rho/\bar{\rho} - 1$ is the gas overdensity, $H(z)$ is the Hubble parameter, ${\rm d}v_{\rm r}/{\rm d}r$ is the gradient of the line-of-sight component of the velocity and all quantities are evaluated at redshift $z = \nu_0/\nu - 1$, where ν_0 is the 21 cm frequency.

Because equation (1) depends on the ionization and temperature as a function of space and time, the 21 cm signal can provide insight into the formation, growth and evolution of structure in the Universe, the nature of the first stars and galaxies and their impact on the physics of the intergalactic medium (IGM; e.g. Barkana & Loeb 2007; Loeb & Furlanetto 2013; Zaroubi 2013). The most widely studied of these properties is the ionization state: in the first billion years, the Universe transitioned from being nearly fully neutral to being nearly fully ionized. This epoch of reionization (EoR) was driven by the percolation of H II regions generated by the ionizing photons escaping from the first galaxies. Sourcing the $x_{\rm H\,I}$ term in equation (1), the EoR should be evidenced by a rise and fall of large-scale fluctuations in the 21 cm brightness temperature (e.g. Lidz et al. 2008).

The second astrophysical term in equation (1) is the IGM spin temperature, $T_{\rm S}$. The spin temperature is thought to be regulated by the first sources of X-rays, which can heat the IGM from its post-thermal decoupling adiabat to temperatures far above the CMB temperature. While the IGM is still adiabatically cooling, the $(1 - T_{\rm CMB}/T_{\rm S})$ term in equation (1) can be of the order of -200. This large dynamic range means that the spatial fluctuations

★E-mail: bradley.greig@sns.it

in temperature during this epoch of heating (EoH) can provide the strongest 21 cm signal, more than an order of magnitude larger than that during the EoR (e.g. Mesinger & Furlanetto 2007; Pritchard & Furlanetto 2007; Baek et al. 2010; Santos et al. 2010; McQuinn & O'Leary 2012; Mesinger, Ferrara & Spiegel 2013). The 21 cm signal can therefore be a powerful probe of high-energy processes in the first galaxies. The most likely of these X-ray sources are high-mass X-ray binaries (HMXBs; Power et al. 2009; Mirabel et al. 2011; Fragos et al. 2013b; Power et al. 2013) and/or the hot interstellar medium (ISM) within the first galaxies (e.g. Oh 2001; Pacucci et al. 2014). However, other alternative scenarios have been put forth including metal-free (Pop-III) stars (Xu et al. 2014), mini-QSOs (e.g. Madau et al. 2004; Yue et al. 2013; Ghara, Choudhury & Datta 2016), dark matter annihilation (e.g. Cirelli, Iocco & Panci 2009; Evoli, Mesinger & Ferrara 2014; Lopez-Honorez et al. 2016) or cosmic rays (Leite et al. 2017).

Numerous 21 cm experiments are currently underway, attempting to detect the cosmic 21 cm signal. These fall into two broad categories. The first are large-scale interferometers, seeking to detect spatial 21 cm fluctuations. These include the Low Frequency Array (van Haarlem et al. 2013; Yatawatta et al. 2013), the Murchison Wide Field Array (Tingay et al. 2013), the Precision Array for Probing the Epoch of Reionization (Parsons et al. 2010), the Square Kilometre Array (SKA; Mellema et al. 2013) and the Hydrogen Epoch of Reionization Array (HERA; DeBoer et al. 2017). The second class are single dipole or small compact array global-sky experiments seeking the volume-averaged global 21 cm signal. These include the Experiment to Detect the Global EoR Signature (Bowman & Rogers 2010), the Sonda Cosmológica de las Islas para la Detección de Hidrógeno Neutro (Voytek et al. 2014), the Shaped Antenna Measurement of the Background Radio Spectrum (Patra et al. 2015), Broadband Instrument for Global HydrOgen ReioNization Signal (Sokolowski et al. 2015), the Large Aperture Experiment to detect the Dark Ages (Greenhill & Bernardi 2012; Bernardi et al. 2016) and the Dark Ages Radio Explorer (Burns et al. 2012).

As a first step in preparation for the wealth of data expected from these 21 cm experiments, we developed a publicly available Monte Carlo Markov Chain (MCMC) EoR analysis tool 21CMMC[1] (Greig & Mesinger 2015). This is the first EoR analysis tool to sample 3D reionization simulations (using 21CMFAST; Mesinger & Furlanetto 2007; Mesinger, Furlanetto & Cen 2011) within a fully Bayesian framework for astrophysical parameter space exploration and 21 cm experiment forecasting. In this introductory work, we adopted the common simplifying assumption of a saturated spin temperature: $T_S \gg T_{CMB}$. However, the applicability of this saturated limit is dependent on the poorly known strength and spectral shape of the X-ray background in the early Universe. If the spin temperature is not fully saturated during the EoR, this could result in sizeable biases in the inferred EoR parameters (e.g. Watkinson & Pritchard 2015).

Beyond its impact on EoR parameter recovery, the IGM spin temperature also encodes a wealth of information on the high-energy processes in the early Universe, as mentioned above. Second-generation interferometers, HERA and SKA, have the bandwidth and sensitivity to easily probe temperature fluctuations during the EoH.

In this work, we extend 21CMMC to include a full treatment of the EoH, retaining our ability to perform on-the-fly sampling of 3D reionization simulations. This updated 21CMMC is capable of jointly exploring the astrophysics of both the EoR and EoH, allowing us to maximize the scientific return of upcoming second-generation telescopes.

We note that recent studies suggest that machine learning can be a viable alternative to on-the-fly MCMC sampling of 21CMFAST. Shimabukuro & Semelin (2017) used an artificial neural network to predict astrophysical parameters, with an accuracy of ∼tens of percent. This approach is fast, though producing Bayesian confidence limits becomes less straightforward. Alternately, Kern et al. (2017) bypassed the on-the-fly sampling of 3D simulations by using an emulator trained on the 21 cm power spectrum (PS). An emulator can be used in an MCMC framework, and is orders of magnitude faster at parameter forecasting compared to a direct sampling of 3D simulations (such as 21CMMC). This comes at the cost of $\lesssim$10 per cent in PS accuracy over most of the parameter space, when the learning is performed on $\sim 10^4$ 21CMFAST training samples (higher precision can be obtained by increasing the size of the training set). Future work will test emulator accuracy on high-order summary statistics.

The remainder of this paper is organized as follows. In Section 2, we summarize 21CMMC and the associated 21CMFAST simulations used to generate 3D realizations of the cosmic 21 cm signal, outlining the updated astrophysical parametrization to model the EoH. In Section 3, we introduce our mock observations to be used in our 21 cm experiment forecasting, and present the forecasts and associated discussions in Section 4. We then explore the impact of assuming the saturated IGM spin temperature limit in Section 5, before summarizing the improvements to 21CMMC and finishing with our closing remarks in Section 6. Unless stated otherwise, we quote all quantities in comoving units and adopt the cosmological parameters: $(\Omega_\Lambda, \Omega_M, \Omega_b, n, \sigma_8, H_0) = (0.69, 0.31, 0.048, 0.97, 0.81, 68\,\mathrm{km\,s^{-1}\,Mpc^{-1}})$, consistent with recent results from the Planck mission (Planck Collaboration XIII 2016).

2 21CMMC

In this section, we provide a short summary of the main aspects of 21CMMC, before delving into the modelling of the cosmic 21 cm signal during the EoR and the EoH in Section 2.1 and developing an intuition about the full parameter set in Section 2.2.

21CMMC is a massively parallel MCMC sampler for exploring the astrophysical parameter space of reionization. It was built using a modified version of the easy to use PYTHON module COSMOHAMMER (Akeret et al. 2013), which employs the EMCEE PYTHON module developed by Foreman-Mackey et al. (2013) based on the affine invariant ensemble sampler of Goodman & Weare (2010). At each proposed step in the computation chain, 21CMMC performs a new, independent 3D reionization of the 21 cm signal, using an optimized version of the publicly available 21CMFAST simulation code (Mesinger & Furlanetto 2007; Mesinger et al. 2011) for computational efficiency. Using a likelihood statistic (fiducially the PS), it compares the model against a mock observation generated from a larger simulation with a different set of initial conditions. For further details, we refer the reader to Greig & Mesinger (2015).

2.1 Modelling the cosmic 21 cm signal with 21CMFAST

In this work, we use an optimized version of the publicly available version of 21CMFAST_v1.1.[2] 21CMFAST employs approximate but efficient modelling of the underlying astrophysics of the reionization

[1] https://github.com/BradGreig/21CMMC

[2] https://github.com/andreimesinger/21cmFAST

and heating epochs. The resulting 21 cm PS during the EoR has been found to match those of computationally expensive radiative transfer simulations to with tens of per cent on the scales relevant to 21 cm interferometry, $\gtrsim$1 Mpc (Zahn et al. 2011). We refer the reader to Mesinger & Furlanetto (2007) and Mesinger et al. (2011) for explicit details on the seminumerical approach, and only provide a summary below.

21CMFAST produces a full, 3D realization of the 21 cm brightness temperature field, $\delta T_{\rm b}$ (cf. equation 1) which is dependent on the ionization, density, velocity and IGM spin temperature fields. The evolved IGM density field at any redshift is obtained from an initial high-resolution linear density field which is perturbed using the Zel'dovich approximation (Zel'dovich 1970) before being smoothed on to a lower resolution grid.

The ionization field is then estimated from this evolved IGM density field using the excursion-set approach (Furlanetto, Zaldarriaga & Hernquist 2004). The time-integrated number of ionizing photons[3] is compared to the number of neutral atoms within regions of decreasing radius, R. These regions are computed from a maximum photon horizon, $R_{\rm mfp}$ down to the individual pixel resolution of a single voxel, $R_{\rm cell}$. A voxel at coordinates $(\boldsymbol{x}, z)$ within the simulation volume is then tagged as fully ionized if,

$$\zeta f_{\rm coll}(\boldsymbol{x}, z, R, \bar{M}_{\rm min}) \geq 1, \tag{2}$$

where $f_{\rm coll}(\boldsymbol{x}, z, R, \bar{M}_{\rm min})$ is the fraction of collapsed matter residing within haloes more massive than $\bar{M}_{\rm min}$ (Press & Schechter 1974; Bond et al. 1991; Lacey & Cole 1993; Sheth & Tormen 1999) and ζ is an ionizing efficiency describing the conversion of mass into ionizing photons (see Section 2.2.1). Partial ionisations are included for voxels not fully ionized by setting their ionized fractions to $\zeta f_{\rm coll}(\boldsymbol{x}, z, R_{\rm cell}, \bar{M}_{\rm min})$.

Since 21 cm observations use the CMB as a background source, the IGM spin temperature has to be coupled to the kinetic gas temperature for the signal to be detected. This coupling is achieved through either collisional coupling or the Lyα background from the first generation of stars [so-called Wouthuysen–Field (WF) coupling (Wouthuysen 1952; Field 1958)]. To compute the spin temperature, 21CMFAST solves for the evolution of the ionization, temperature and impinging Lyα background in each voxel.[4] These depend on the angle-averaged specific intensity, $J(\boldsymbol{x}, E, z)$, (in erg s^{-1} keV^{-1} cm^{-2} sr^{-1}), computed by integrating the comoving X-ray specific emissivity, $\epsilon_{\rm X}(\boldsymbol{x}, E_e, z')$ back along the light-cone:

$$J(\boldsymbol{x}, E, z) = \frac{(1+z)^3}{4\pi} \int_z^\infty {\rm d}z' \frac{c\,{\rm d}t}{{\rm d}z'} \epsilon_{\rm X} e^{-\tau}. \tag{3}$$

Here, $e^{-\tau}$ corresponds to the probability that a photon emitted at an earlier time, z', survives until z owing to IGM attenuation (see equation 16 of Mesinger et al. 2011) and the comoving specific emissivity is evaluated in the emitted frame, $E_{\rm e} = E(1+z')/(1+z)$, with

$$\epsilon_{\rm X}(\boldsymbol{x}, E_{\rm e}, z') = \frac{L_{\rm X}}{\rm SFR} \left[\rho_{\rm crit,0} \Omega_b f_* (1+\delta_{\rm nl}) \frac{{\rm d}f_{\rm coll}(z')}{{\rm d}t}\right], \tag{4}$$

where the quantity in square brackets is the star formation rate (SFR) density along the light-cone, with $\rho_{\rm crit,0}$ being the current critical density and f_* the fraction of galactic baryons converted into stars.

The quantity $L_{\rm X}/{\rm SFR}$ is the specific X-ray luminosity per unit star formation escaping the galaxies (in units of erg s^{-1} keV^{-1} M$_\odot^{-1}$ yr). The specific luminosity is taken to be a power law in photon energy, $L_{\rm X} \propto E^{-\alpha_{\rm X}}$, with photons below some threshold energy, E_0, being absorbed inside the host galaxy.[5]

Instead of the number of X-ray photons per stellar baryon used in the default version of 21CMFAST, here we normalize the X-ray efficiency in terms of an integrated soft-band (<2 keV) luminosity per SFR (in erg s^{-1} M$_\odot^{-1}$ yr):

$$L_{\rm X<2\,keV}/{\rm SFR} = \int_{E_0}^{2\,{\rm keV}} {\rm d}E_e L_{\rm X}/{\rm SFR}. \tag{5}$$

This parametrization is both physically motivated (harder photons have mean free paths longer than the Hubble length and so do not contribute to the EoH; e.g. McQuinn 2012; Das et al. 2017) and easier to directly compare with X-ray observations of local star-forming galaxies.

2.2 The 21CMMC astrophysical parameter set

In the previous section, we outlined the seminumerical approach, using 21CMFAST, to obtain the 3D realizations of the 21 cm brightness temperature field. This parametrization yields six free parameters to be sampled within our Bayesian framework. In this section, we provide more detailed descriptions for each of these parameters, providing physical intuition for their impact on the IGM through X-ray heating or ionization and defining their allowed ranges.

To aid in this discussion, we provide Fig. 1. For each parameter, denoted (i)–(vi), we provide the redshift evolution of the corresponding average neutral fraction (*top panel*), average 21 cm brightness temperature contrast (*middle panel*) and the amplitude of the 21 cm PS at $k = 0.15\,{\rm Mpc}^{-1}$ (*bottom panel*)[6] $(\delta\bar{T}_{\rm b}^2 \Delta_{21}^2(k,z) \equiv k^3/(2\pi^2 V)\, \delta\bar{T}_{\rm b}^2(z)\, \langle|\delta_{21}(\boldsymbol{k},z)|^2\rangle_k$ where $\delta_{21}(\boldsymbol{x},z) \equiv \delta T_{\rm b}(\boldsymbol{x},z)/\delta\bar{T}_{\rm b}(z) - 1$). In each set of panels, we vary the astrophysical parameter in question across its full allowed span, holding the other five parameters fixed.

The solid, black curve in each panel corresponds to our 'fiducial' FAINT GALAXIES model (see Section 3 for further details). Before discussing the impact of each parameter, it is instructive to note the general features exhibited by the fiducial model. The EoR history

[3] This includes ionizations from both UV and X-ray sources. While X-rays can produce some level of pre-reionization (e.g. Ricotti & Ostriker 2004; Dijkstra et al. 2012; McQuinn 2012; Mesinger et al. 2013) their predominant contribution is in pre-heating of the IGM before reionization (e.g. McQuinn & O'Leary 2012).

[4] Note that within this work we do not vary the soft UV spectra of the first sources driving this epoch. This WF coupling epoch will be extremely challenging to detect in comparison to the EoR and the EoH. Nevertheless, we will return to this in future work. For more specifics regarding the computation of the Lyα background, we refer the reader to section 3.2 of Mesinger et al. (2011)

[5] We note that in the computation of the heating and ionization rates in the default version of 21CMFAST, these integrals were performed out to infinity, which could result in divergent behaviour for $\alpha_{\rm X} \leq 0$. Here, we adopt an upper limit of 10 keV for computing the rate integrals. This choice is arbitrary and purely for numerical convenience, as the EoH only depends on the SED below $\sim$2 keV. Actual SEDs of course do not diverge but turn over at high energies: $\sim$10–100 keV (e.g. Lehmer et al. 2013, 2015).

[6] Our choice of k-modes was motivated by the fact that the large-scale power in the 21 cm PS is the main discriminant between astrophysical models (e.g. McQuinn et al. 2007; Greig & Mesinger 2015), Moreover, these k-modes are detectable by upcoming experiments (i.e. they are sufficiently small to avoid being contaminated by foregrounds yet large enough to obtain high signal to noise).

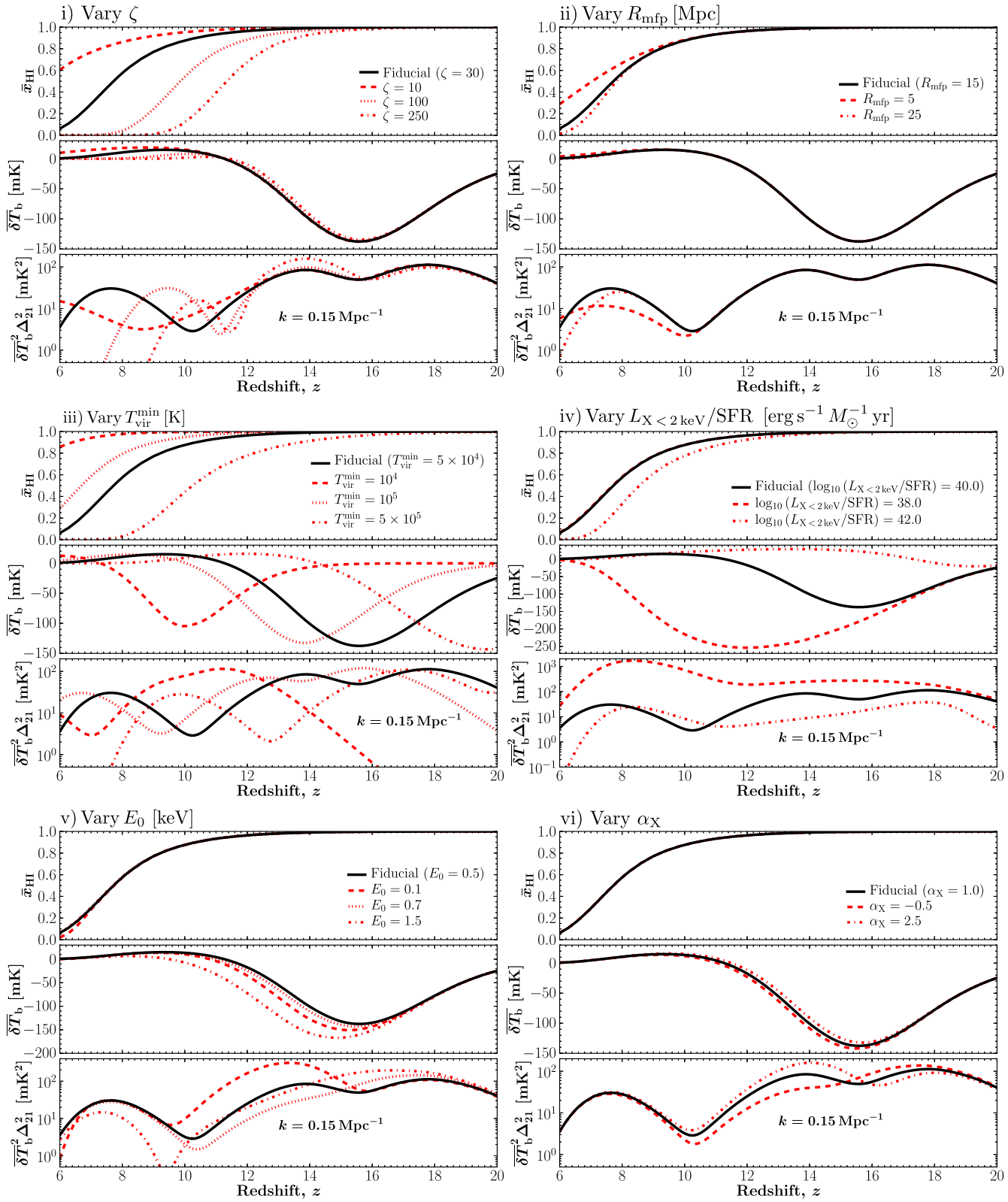

Figure 1. The impact of each of our six astrophysical model parameters on the evolution of the IGM neutral fraction (top panel), global averaged 21 cm brightness temperature contrast (middle panel) and the evolution of the PS amplitude at $k = 0.15\,{\rm Mpc}^{-1}$ (bottom panel). We vary each model parameter across the full allowed prior range, holding the remaining five parameters fixed to the fiducial FAINT GALAXIES model values (see Section 3).

in the top panel has a monotonic evolution with a mid-point around $z \sim 8$. The global 21 cm signal in the middle panel shows a deep absorption trough, corresponding to when the X-ray heating rate surpasses the adiabatic cooling rate (start of the EoH). This is followed by a small emission peak, corresponding to the onset of the EoR (e.g. Furlanetto 2006). The height of the peak is determined by the relative overlap of the EoR and EoH; if the overlap is strong, reionization can proceed in a cold IGM, with the global signal never switching to emission.

The large-scale power in the bottom panel shows the characteristic three-peaked structure, driven by fluctuations in the Ly α background (WF coupling), IGM gas temperature (EoH) and the ionization fraction (EoR), from right to left, respectively (e.g. Pritchard & Furlanetto 2007; Baek et al. 2010). The redshift position of each peak therefore traces the timing of each epoch, while the amplitude of the 21 cm power traces the level of fluctuations determined by the typical source bias and/or X-ray SED (e.g. Mesinger et al. 2013). Troughs on the other hand correspond to the transitions between epochs, when the corresponding cross terms of the 21 cm PS cause the large-scale power to drop (e.g. Lidz et al. 2007; Pritchard & Furlanetto 2007; Mesinger, Greig & Sobacchi 2016).

2.2.1 *UV ionizing efficiency, ζ*

The UV ionizing efficiency of high-z galaxies (equation 2) can be expressed as

$$\zeta = 30 \left(\frac{f_{\rm esc}}{0.12}\right) \left(\frac{f_*}{0.05}\right) \left(\frac{N_{\gamma/b}}{4000}\right) \left(\frac{1.5}{1+n_{\rm rec}}\right), \quad (6)$$

where $f_{\rm esc}$ is the fraction of ionizing photons escaping into the IGM, f_* is the fraction of galactic gas in stars, $N_{\gamma/b}$ is the number of ionizing photons produced per baryon in stars and $n_{\rm rec}$ is the typical number of times a hydrogen atom recombines. While only the product of equation (6) is required for generating the ionization field, we provide some plausible values for each of the terms. We adopt $N_\gamma \approx 4000$ as is typically expected from Population II stars (e.g. Barkana & Loeb 2005). For high-z galaxies, both $f_\star$ and $f_{\rm esc}$ are extremely uncertain, with observations and simulations placing plausible values within the vicinity of $\sim$10 per cent for $f_\star$ (e.g. Behroozi & Silk 2015; Sun & Furlanetto 2016) and $f_{\rm esc}$ (e.g. Paardekooper, Khochfar & Dalla Vecchia 2015; Xu et al. 2016; Kimm et al. 2017). Finally, we adopt $n_{\rm rec} \sim 0.5$, similar to those found in the 'photon-starved' reionization models of Sobacchi & Mesinger (2014), which are consistent with emissivity estimates from the Ly α forest (e.g. Bolton & Haehnelt 2007; McQuinn, Oh & Faucher-Giguère 2011). It is important to note that the $f_\star$ appearing here, is equivalent to the $f_\star$ in equation (4). That is, throughout all cosmic epochs, we adopt the same, constant value of 5 per cent for the fraction of galactic gas in stars. In future work, we will relax this assumption.

In this work, we adopt a flat prior over the fiducial range of $\zeta \in [10, 250]$, which is a notable extension over the original upper limit of $\zeta = 100$ chosen in Greig & Mesinger (2015). The extended range provides the flexibility to explore physically plausible models where reionization is driven by bright, rare galaxies (see Section 3). In panel (i) of Fig. 1, we highlight the impact of varying ζ. As expected, ζ has a strong impact on the EoR and an almost negligible impact on the EoH. As ζ is increased, the EoR peak shifts to earlier redshifts and the width of the EoR peak reduces (i.e. shorter duration). For extremely large values of ζ, the EoR and EoH peaks begin to merge, resulting in a larger amplitude EoR peak, sourced by the contrast between the cold IGM patches present in the early EoH stages and the H II regions.

2.2.2 *Maximum ionizing photon horizon within ionized regions, $R_{\rm mfp}$*

The physical size of H II regions is regulated by the distance ionizing photons can propagate into the IGM. This depends on the abundance of photon sinks (absorption systems such as Lyman limit systems) and the corresponding recombinations of these systems. When the H II regions start approaching the typical separation of the photon sinks, an increasing fraction of ionizing photons are used to balance recombinations, and the EoR can slow down (e.g. Furlanetto & Oh 2005; Furlanetto & Mesinger 2009; Alvarez & Abel 2012).

The details of this process can be complicated (e.g. Sobacchi & Mesinger 2014); however, a common simplification in seminumerical approaches is to adopt a maximum horizon for the ionizing photons within the ionized IGM, $R_{\rm mfp}$,[7] which is implemented as the maximum filtering scale in the excursion-set EoR modelling (see Section 2.1). Motivated by recent subgrid recombination models (Sobacchi & Mesinger 2014), we adopt a flat prior over $R_{\rm mfp} \in [5, 25]$ cMpc.

In panel (ii) of Fig. 1, we show the impact of $R_{\rm mfp}$ over cosmic history. As mentioned above, $R_{\rm mfp}$ only becomes important in the advanced stages of reionization, when the typical H II region scale approaches $R_{\rm mfp}$. The result is a delay of the late stages of the EoR for small values of $R_{\rm mfp}$. Limiting the photon horizon with a decreasing $R_{\rm mfp}$ ($\lesssim$15 Mpc) is also evidenced by a drop in the large-scale 21 cm PS (e.g. McQuinn et al. 2007; Alvarez & Abel 2012; Mesinger, McQuinn & Spergel 2012; Greig & Mesinger 2015). Values of $R_{\rm mfp} > 15$ Mpc have little impact on the 21 cm PS (for this combination of the other astrophysical parameters), as the clustering of the ionizing sources becomes the dominant source of power (note the same PS amplitude for $R_{\rm mfp} = 15$ and 25 Mpc).

2.2.3 *Minimum virial temperature of star-forming haloes, $T_{\rm vir}^{\rm min}$*

We define the minimum threshold for a halo hosting a star-forming galaxy to be its virial temperature, $T_{\rm vir}^{\rm min}$, which is related to the halo mass via, (e.g. Barkana & Loeb 2001)

$$M_{\rm vir}^{\rm min} = 10^8 h^{-1} \left(\frac{\mu}{0.6}\right)^{-3/2} \left(\frac{\Omega_{\rm m}}{\Omega_{\rm m}^z} \frac{\Delta_{\rm c}}{18\pi^2}\right)^{-1/2} \times \left(\frac{T_{\rm vir}^{\rm min}}{1.98 \times 10^4 {\rm K}}\right)^{3/2} \left(\frac{1+z}{10}\right)^{-3/2} {\rm M}_\odot, \quad (7)$$

where μ is the mean molecular weight, $\Omega_{\rm m}^z = \Omega_{\rm m}(1+z)^3/[\Omega_{\rm m}(1+z)^3 + \Omega_\Lambda]$, and $\Delta_c = 18\pi^2 + 82d - 39d^2$ where $d = \Omega_{\rm m}^z - 1$. The choice of $T_{\rm vir}^{\rm min}$ acts as a step-function cut-off to the UV luminosity function. Below $T_{\rm vir}^{\rm min}$, it is assumed that internal feedback mechanisms such as supernova or photoheating suppress the formation of stars. Above, efficient star formation overcomes internal feedback, enabling these haloes to produce ionizing photons capable of

[7] For historical context, we adopt '$R_{\rm mfp}$' to denote this effective horizon set by subgrid recombinations. The subgrid models of Sobacchi & Mesinger (2014) do not translate to a constant, uniform value of $R_{\rm mfp}$, and further the mean free path is typically larger than $R_{\rm mfp}$ (since the former is an instantaneous quantity while the latter depends on the cumulative contributions of subgrid recombinations). However, these authors find that the approximation of a constant $R_{\rm mfp}$ can reproduce the 21 cm PS of their fiducial model to $\sim$10 per cent. Future versions of 21CMMC will include the Sobacchi & Mesinger (2014) subgrid recombination model, eliminating $R_{\rm mfp}$ as a free parameter.

contributing to the EoR and EoH. We shall consider a flat prior across $T_{\rm vir}^{\rm min} \in [10^4, 10^6]$ K within this work.

Our lower limit, $T_{\rm vir}^{\rm min} \approx 10^4$ K, is motivated by the minimum temperature for efficient atomic line cooling. In principle, $T_{\rm vir}^{\rm min}$ can be as low as $\approx 10^2$ K in the presence of radiative cooling (Haiman, Thoul & Loeb 1996; Tegmark et al. 1997; Abel, Bryan & Norman 2002; Bromm, Coppi & Larson 2002), however, star formation within these haloes is likely inefficient (a few stars per halo; e.g. Kimm et al. 2017) and can quickly ($z > 20$) be suppressed by Lyman–Werner or other feedback processes well before the EoR (Haiman, Abel & Rees 2000; Ricotti, Gnedin & Shull 2001; Haiman & Bryan 2006; Mesinger, Bryan & Haiman 2006; Holzbauer & Furlanetto 2012; Fialkov et al. 2013). Our upper limit of $T_{\rm vir}^{\rm min} \approx 10^6$ K is roughly consistent with the host halo masses of observed Lyman break galaxies at $z \sim 6$–8, as estimated with the abundance matching technique (e.g. Kuhlen & Faucher-Giguère 2012; Barone-Nugent et al. 2014).

Note that within the 21CMFAST framework, $T_{\rm vir}^{\rm min}$ is important both in the EoR and EoH, determining the ionization field ($f_{\rm coll}$, equation 2) and the specific emissivity requisite for the X-ray heating background ($\frac{{\rm d}f_{\rm coll}}{{\rm d}t}$, equation 4), respectively. This implies that the efficient star-forming galaxies responsible for reionization are the same galaxies that host the sources responsible for X-ray heating (i.e. the physics of star formation drives both the X-ray heating and ionization fields). As a result, $T_{\rm vir}^{\rm min}$ affects the timing of both the EoR and EoH.

This is evident in panel (iii) of Fig. 1. The EoR and EoH milestones are pushed to lower redshifts for an increasing $T_{\rm vir}^{\rm min}$. For a suitably large choice of $T_{\rm vir}^{\rm min}$ (e.g. 5×10^5 K), the timing of the EoH and WF coupling peaks can be sufficiently delayed to result in their overlap. In addition to the timing, $T_{\rm vir}^{\rm min}$ also impacts the amplitude of the fluctuations. Rarer (more biased) galaxies, corresponding to larger values of $T_{\rm vir}^{\rm min}$, are evidenced by more 21 cm power at a given epoch (e.g. McQuinn et al. 2007).

2.2.4 *Integrated soft-band luminosity,* $L_{X<2\,{\rm keV}}/SFR$

The efficiency of X-ray heating is driven by the total integrated soft-band (<2 keV) luminosity per SFR (equation 5) escaping into the IGM, which normalizes the emergent specific emissivity produced by the X-ray sources within the first galaxies. Within this work, we adopt a flat prior over the range $\log_{10}(L_{X<2\,{\rm keV}}/{\rm SFR}) \in [38, 42]$. This range is conservatively selected[8] to be one to two orders of magnitude broader than the distribution seen in local populations of star-forming galaxies (Mineo, Gilfanov & Sunyaev 2012a), and their stacked *Chandra* observations (Lehmer et al. 2016). It also encompasses values at high redshifts predicted by population synthesis models (Fragos et al. 2013a).

In Panel (iv) of Fig. 1, we highlight the impact of $L_{X<2\,{\rm keV}}/{\rm SFR}$. For very high values of $L_{X<2\,{\rm keV}}/{\rm SFR}$, the EoH commences prior to the completion of WF coupling. As a result, no strong absorption feature in $\delta\bar{T}_{\rm b}$ is observed, and the Lyα–EoH peaks in the 21 cm PS merge. In addition to heating, such high X-ray luminosities can also substantially ionize the EoR (at ∼10–20 per cent level). In this case, the EoR can complete earlier (top panel).

[8] It is also roughly consistent with the limits proposed by Fialkov et al. (2017) using observations of the unresolved cosmic X-ray background (e.g. Lehmer et al. 2012) and the upper limits on the measured 21 cm PS from PAPER-64 (e.g. Ali et al. 2015; Pober et al. 2015).

At the other end of the range, extremely inefficient X-ray heating (dashed curve) results in a delayed EoH, with the EoR and EoH overlapping. In this 'cold reionization' scenario (Mesinger et al. 2013), reionization proceeds in an IGM which is significantly colder than the CMB. The resultant large temperature contrasts between the ionized H II regions and cold neutral IGM can yield an extremely large 21 cm PS amplitude (∼10^3 mK^2).[9]

2.2.5 *X-ray energy threshold for self-absorption by the host galaxies,* E_0

The soft X-rays produced within galaxies can be absorbed by the intervening ISM, thus not being able to escape and contribute to heating the IGM. The impact that this ISM absorption has on the emergent X-ray SED depends on the ISM density and metallicity. Early galaxies responsible for the EoH are expected to be less polluted by metals than local analogues. Indeed, Das et al. (2017) find that the emergent X-ray SED from simulated high-redshift galaxies can be well approximated by a metal-free ISM with a typical column density of $\log_{10}(N_{\rm H\,I}/{\rm cm}^2) = 21.40^{+0.40}_{-0.65}$. As the opacity of metal-free gas is a steep function of energy, these authors find that the 21 cm PS from the emerging X-ray SED can be well approximated using the common assumption of a step function attenuation of the X-ray SED below an energy threshold, E_0. In this work, we adopt a flat prior over $E_0 \in [0.1, 1.5]$ keV which corresponds to $\log_{10}(N_{\rm H\,I}/{\rm cm}^2) \in [19.3, 23.0]$[10].

Panel (v) of Fig. 1 highlights the impact of E_0. As $L_{X<2\,{\rm keV}}/{\rm SFR}$ defines the total soft-band luminosity, as we increase (decrease) E_0 we effectively harden (soften) the spectrum of emergent X-ray photons. Since the absorption cross-section scales as $\propto E^{-3}$, we would naively expect smaller values of E_0 to result in more efficient heating, shifting the minimum in the global signal to higher redshifts. However, this evolution is slightly reversed for very low values, $E_0 \lesssim 0.5$ keV, since the energy of these very soft photons is continually deposited in a limited volume surrounding the first galaxies; thus, the volume-averaged global signal during the EoH is slightly delayed for these very soft SEDs. This highlights the need to properly model the spatially dependent IGM heating, even when predicting the average signal.

The amplitude of the PS is very highly dependent on E_0. Softer SEDs result in very inhomogeneous heating, with PS amplitudes larger by up to an order of magnitude (e.g. Pacucci et al. 2014). The amplitude of the EoH peak consistently decreases for an increasing E_0, as the harder SEDs make the EoH more homogeneous. Eventually for $E_0 > 0.7$ keV, no EoH peak occurs, as the large mean free path of the X-ray photons result in an inefficient, relatively uniform heating of the IGM (e.g. Fialkov, Barkana & Visbal 2014).

2.2.6 *X-ray spectral index,* $\alpha_{\rm X}$

The spectral index, $\alpha_{\rm X}$, describing the emergent spectrum from the first galaxies hosting X-ray sources depends on what is assumed to be the dominant process producing X-ray photons. In this work, we

[9] Though the specific model shown here exceeds the PAPER-64 upper limits, for other choices of the EoR and EoH parameters, this same choice of $L_{X<2\,{\rm keV}}/{\rm SFR} = 10^{38}$ erg s^{-1} M$_\odot^{-1}$ yr can result in a 21 cm PS below these upper limits.

[10] The conversion to column densities is computed assuming a unity optical depth for a pristine, metal-free, neutral ISM (i.e. the contribution from He II is negligible).

adopt a fiducial flat prior of $\alpha_X \in [-0.5, 2.5]$ which should encompass the most relevant high-energy X-ray SEDs that describe the first galaxies (e.g. HMXBs, host ISM, mini-quasars, SNe remnants etc.; see e.g. McQuinn 2012; Pacucci et al. 2014).

Finally, in panel (vi) of Fig. 1, we illustrate the impact of α_X. For an increasing α_X, more soft X-ray photons are produced (as the soft-band luminosity is kept fixed) resulting in more efficient X-ray heating. This results in an increase in the temperature fluctuations, driving a larger amplitude of the EoH peak in the 21 cm PS. Conversely, for an inverted spectral index, $\alpha_X = -0.5$, the emergent X-ray photons are spectrally harder, producing inefficient uniform X-ray heating, and limited temperature fluctuations. Thus, the EoH peak in the 21 cm PS for $\alpha_X = -0.5$ (dashed curve) is suppressed. However, over our adopted range of priors, the absorption by the host galaxy, E_0, is much more potent in hardening/softening the SED than the spectral index, α_X.

2.3 Telescope noise profiles

In order to provide astrophysical parameter forecasting, we must model the expected noise of the 21 cm experiments. Within this work, we focus solely on the 21 cm PS. To generate the sensitivity curves for 21 cm interferometer experiments, we use the PYTHON module 21CMSENSE[11] (Pober et al. 2013, 2014). Below, we summarize the main aspects and assumptions required to produce telescope noise profiles.

First, the thermal noise PS is calculated at each gridded uv-cell according to the following (e.g. Morales 2005; McQuinn et al. 2006; Pober et al. 2014):

$$\Delta^2_N(k) \approx X^2 Y \frac{k^3}{2\pi^2} \frac{\Omega'}{2t} T^2_{sys}, \tag{8}$$

where X^2Y is a cosmological conversion factor between the observing bandwidth, frequency and comoving distance, Ω' is a beam-dependent factor derived in Parsons et al. (2014), t is the total time spent by all baselines within a particular k-mode and T_{sys} is the system temperature, the sum of the receiver temperature, T_{rec}, and the sky temperature T_{sky}. We model T_{sky} using the frequency-dependent scaling $T_{sky} = 60 \left(\frac{\nu}{300\,\mathrm{MHz}}\right)^{-2.55}$ K (Thompson, Moran & Swenson 2001).

The sample variance of the cosmological 21 cm PS can easily be combined with the thermal noise to produce the total noise PS using an inverse-weighted summation over all the individual modes (Pober et al. 2013),

$$\delta\Delta^2_{T+S}(k) = \left(\sum_i \frac{1}{(\Delta^2_{N,i}(k) + \Delta^2_{21}(k))^2} \right)^{-1/2}, \tag{9}$$

where $\delta\Delta^2_{T+S}(k)$ is the total uncertainty from thermal noise and sample variance in a given k-mode and $\Delta^2_{21}(k)$ is the cosmological 21 cm PS (mock observation). Here, we assume Gaussian errors for the cosmic-variance term, which is a good approximation on large scales.

The largest primary uncertainty for 21 cm experiments is dealing with the bright foreground contamination. However, for the most part these bright foregrounds are spectrally smooth and have been shown to reside within a confined region of cylindrical 2D k-space known as the 'wedge' (Datta, Bowman & Carilli 2010; Morales et al. 2012; Parsons et al. 2012b; Trott, Wayth & Tingay 2012; Vedantham, Shankar & Subrahmanyan 2012; Hazelton, Morales & Sullivan 2013; Thyagarajan et al. 2013; Liu, Parsons & Trott 2014a,b; Thyagarajan et al. 2015a,b; Pober et al. 2016). Outside of this 'wedge', we are left with a relatively pristine observing window where the cosmic 21 cm signal is only affected by the instrumental thermal noise. At present, the location of the boundary separating this observing window and the 'wedge'-like feature is uncertain.

Within 21CMSENSE three foreground removal strategies are provided (Pober et al. 2014), 'optimistic', 'moderate' and 'pessimistic'. We defer the reader to this work for further details on these scenarios, highlighting here that we choose to adopt the 'moderate' scenario. This entails 21 cm observations only within the pristine 21 cm window (i.e. avoiding the 'wedge'), with the wedge location defined to extend $\Delta k_\parallel = 0.1\,h\,\mathrm{Mpc}^{-1}$ beyond the horizon limit (Pober et al. 2014). Furthermore, this scenario includes the coherent summation over all redundant baselines within the array configuration allowing the reduction of thermal noise (Parsons et al. 2012a).

Within this work, we focus on the two second-generation 21 cm interferometer experiments capable of simultaneously measuring the EoR and the EoH, namely the SKA and HERA. Below (and in Table 1) we summarize the specific design features and assumptions required to model the theoretical noise of both instruments:

1. *HERA:* We follow the design specifics outlined in Beardsley et al. (2015) with a core design consisting of 331 dishes.[12] Each dish is 14 m in diameter closely packed into a hexagonal configuration to maximize the total number of redundant baselines (Parsons et al. 2012a). We model the total system temperature as $T_{sys} = 100 + T_{sky}$K. HERA will operate in a drift-scanning mode, for which we assume a total 1080 h observation, spread across 180 nights at 6 h per night.
2. *SKA:* We use the latest[13] available design for SKA-low Phase 1, using the telescope positions provided in the most recent SKA System Baseline Design document.[14] Specifically, SKA-low Phase 1 includes a total of 512 35 m antenna stations randomly distributed within a 500 m core radius. The total SKA system

Table 1. Summary of telescope parameters we use to compute sensitivity profiles (see the text for further details).

Parameter	HERA	SKA
Telescope antennas	331	512
Diameter (m)	14	35
Collecting Area (m^2)	50 953	492 602
T_{rec} (K)	100	$0.1T_{sky} + 40$
Bandwidth (MHz)	8	8
Integration time (h)	1000 (drift)	1000 (tracked)

[11] https://github.com/jpober/21cmSense

[12] Note, the final fully funded design for HERA consists of 350 dishes, 320 in the core and 30 outriggers (DeBoer et al. 2017). For all intents and purpose for this work, the difference between a 320 and 331 core layout is negligible.

[13] In Greig & Mesinger (2015), we used the original design prior to the re-baselining (the 50 per cent reduction in the number of antenna dipoles), while in Greig, Mesinger & Koopmans (2015) we investigated several design layouts to maximize the sensitivity specifically for the 21 cm PS following the re-baselining. The latest design for the SKA results in reduced sensitivity when compared to both our previous works, and therefore we caution comparisons between the SKA within this work and our previous studies.

[14] http://astronomers.skatelescope.org/wp-content/uploads/2016/09/SKA-TEL-SKO-0000422_02_SKA1_LowConfigurationCoordinates-1.pdf

Table 2. A summary of the astrophysical parameters used for our two mock observations, the corresponding electron scattering optical depth, τ_e, as well as the adopted prior range for 21CMMC. See the text for additional details.

Source model	ζ	$R_{\rm mfp}$ (Mpc)	$T_{\rm vir}^{\rm min}$ (K)	$\log_{10}(T_{\rm vir}^{\rm min})$ (K)	$\log_{10}(L_{X<2\,{\rm keV}}/{\rm SFR})$ (erg s^{-1} M$_\odot^{-1}$ yr)	E_0 (keV)	$\log_{10}(N_{\rm H\,I})$ (cm^{-2})	α_X	τ_e
FAINT GALAXIES	30.0	15.0	5×10^4	4.70	40.0	0.5	21.45	1.0	0.059
BRIGHT GALAXIES	200.0	15.0	3×10^5	5.48	40.0	0.5	21.45	1.0	0.056
Allowed range	[10, 250]	[5, 25]	[10^4, 10^6]	[4.0, 6.0]	[38.0, 42.0]	[0.1, 1.5]	[19.3,23.0]	[−0.5, 2.5]	

temperature is modelled as outlined in the SKA System Baseline Design, $T_{\rm sys} = 1.1T_{\rm sky} + 40$K. For the SKA we adopt a single, deep 1000 h tracked scan of a cold patch on the sky.

It is non-trivial to perform a like-for-like comparison between the two experiments, as HERA intends to perform a rotational synthesis drift scan, whereas the SKA intends to conduct track scanned observations.[15] These two strategies result in considerably different noise PS. A single tracked field with the SKA will have considerably lower thermal noise than HERA owing to the deeper integration time, and therefore SKA will be superior on small scales (large k) important for imaging. On the other hand, by observing numerous patches of the sky rotating through the zenith pointing field of view of HERA per night, sample variance can be better mitigated compared to the single tracked field of the SKA (i.e. HERA will have reduced noise on large scales, small k). For the most part, the strongest constraints on the astrophysical parameters come from the large-scale (small k) modes of the 21 cm PS, and therefore using the PS as the likelihood statistic will favour the approach of HERA over that of SKA. We quantify these claims further in the Appendix, showing the noise power spectra at different redshifts.

Further complicating a direct comparison is the fact that the SKA is planning a tiered survey. For simplicity, in this introductory work we only consider a single, deep 1000 h observation (though we will return to this in the future). However, we could have considered either the intermediate 10 × 100 h or wide and shallow 100 × 10 h strategies (e.g. Greig et al. 2015). These latter two surveys concede thermal noise sensitivity (from the reduced per field integration time) for an increased sample variance sensitivity by surveying multiple fields. In terms of the simplified three parameter EoR model considered in Greig & Mesinger (2015), the single, deep 1000 h observation recovered the largest uncertainties on the astrophysical parameters relative to the intermediate or wide and shallow surveys (i.e. a single, tracked field was the worst performed strategy).

3 MOCK COSMIC SIGNAL

Having outlined our astrophysical model to describe the EoR and EoH, we now introduce our mock observations of the cosmic 21 cm signal. It is impractical to vary all available astrophysical parameters when creating mock observations, and therefore, following Mesinger et al. (2016) we take two extreme choices for $T_{\rm vir}^{\rm min}$. This parameter characterizes both the timing of the epochs and the typical bias of the dominant galaxies, thus encoding the largest variation in the 21 cm signal [e.g panel (iii) of Fig. 1]. Specifically, we adopt $T_{\rm vir}^{\rm min} = 5 \times 10^4$ K (FAINT GALAXIES) and $T_{\rm vir}^{\rm min} = 3 \times 10^5$ K (BRIGHT GALAXIES). These choices approximately match the evolution of the cosmic SFR density inferred from extrapolating the observed luminosity functions[16] (Bouwens et al. 2015) down to a UV magnitude of $M_{\rm UV} = -10\,(-17)$ for the FAINT GALAXIES (BRIGHT GALAXIES) model (see fig. 5 of Das et al. 2017).

In order to match the latest constraints on the electron scattering optical depth, τ_e, from Planck ($\tau_e = 0.058 \pm 0.012$; Planck Collaboration XLVII 2016), we adopt $\zeta = 30$ for the FAINT GALAXIES model. This corresponds to the fiducial parameter set outlined in equation (6). For the biased, rarer galaxies in the BRIGHT GALAXIES model, we adopt $\zeta = 200$. We select a fiducial $R_{\rm mfp} = 15$ Mpc for both models. In Table 2, we summarize the adopted astrophysical parameter set for each of the two models, while also providing the corresponding optical depth, τ_e.

We adopt the same X-ray source model for both the BRIGHT GALAXIES and FAINT GALAXIES models. We assume HMXBs to be the dominant X-ray heating source within the first galaxies, and use the results of Das et al. (2017) to describe the emergent X-ray SED.[17] This corresponds to an energy threshold, $E_0 = 0.5$ keV ($\log_{10}(N_{\rm H\,I}/{\rm cm}^2) = 21.5$) and an X-ray spectral index of $\alpha_X = 1.0$. Finally, we assume an HMXB soft-band luminosity of $L_{X<2\,{\rm keV}}/{\rm SFR} = 10^{40}\,{\rm erg\,s^{-1}\,M_\odot^{-1}\,yr}$, which is consistent with estimates from the HMXB population synthesis models of Fragos et al. (2013a).

In Fig. 2, we provide the cosmic evolution of our two EoR source models: FAINT GALAXIES (solid curve) and BRIGHT GALAXIES (dashed curve). The top, middle and bottom panels are the global reionization history, global 21 cm signal and the 21 cm PS at $k = 0.15$ (black) and $k = 0.5\,{\rm Mpc}^{-1}$ (red), respectively. These show qualitatively the same behaviour as we have discussed in the previous section. These mock observations are generated from simulations with a volume of $600^3\,{\rm Mpc}^3$, on a 400^3 grid smoothed down from the high-resolution initial conditions generated on a 2400^3 grid.

By construction, these two EoR models have a similar reionization history, consistent with the latest observations. The FAINT GALAXIES model has a somewhat more extended EoR, as the less biased DM haloes that host the dominant galaxies form slower. Unlike for the observationally constrained EoR history, we allow the EoH history to be different in the two models. In other words, we take

[15] Additionally, HERA is a dedicated 21 cm experiment specifically designed for a 21 cm PS measurement, while the SKA is a multidisciplinary experiment, with detection of the 21 cm signal only one of many key science goals. Moreover, the instrument layout and design is tailored towards 3D tomographic imaging (e.g. Mellema et al. 2013) rather than the 21 cm PS.

[16] In the future, we will provide a more generalized parametrization of the ionizing source model by allowing each individual constituent of ζ (equation 6) to vary with halo mass (Park et al., in preparation). This will enable additional flexibility in the source modelling, while at the same time allowing high-z galaxy luminosity functions to be applied as priors to the source model prescription.

[17] Note that the typical star-forming haloes used by Das et al. (2017), e.g. $\lesssim 3 \times 10^8\,{\rm M}_\odot$, are smaller than the corresponding masses set by our minimum on $T_{\rm vir}^{\rm min}$ (e.g. 10^4 K). Therefore, we have assumed that the intrinsic attenuation is independent of the host galaxy mass. This, however, need not be the case.

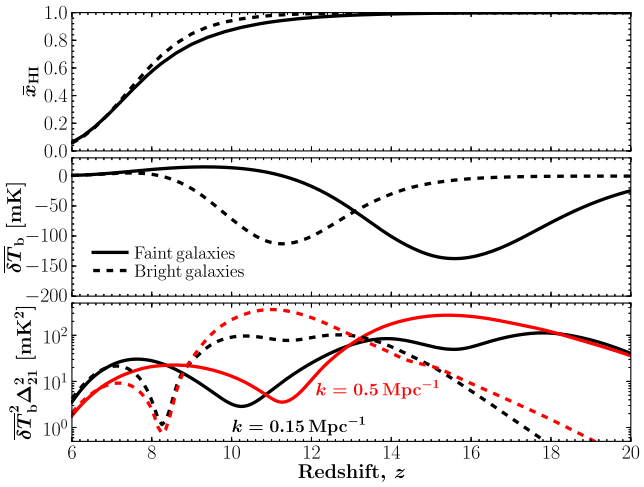

Figure 2. Cosmic evolution of the BRIGHT GALAXIES (dashed) and FAINT GALAXIES (solid) models used for the mock observations within this work. *Top:* the evolution of the IGM neutral fraction. *Middle:* global averaged 21 cm brightness temperature contrast. *Bottom:* evolution of the PS amplitude at two different k-modes, $k = 0.15\,{\rm Mpc}^{-1}$ (black) and $k = 0.5\,{\rm Mpc}^{-1}$ (red).

the same X-ray luminosity per SFR. As a result, the FAINT GALAXIES model has an earlier EoH (see the middle panel), governed by the formation of the first $T_{\rm vir}^{\rm min} = 5 \times 10^4$ K structures.

Due to this, these two models will be interesting for our astrophysical parameter forecasting for both HERA and SKA. With a decreasing sensitivity with increasing redshift, the location of the EoR and EoH peaks will impact the resultant significance of a detection of the 21 cm signal. For example, in the bottom panel of Fig. 2, it is evident that the BRIGHT GALAXIES model exhibits additional 21 cm power relative to the FAINT GALAXIES model. Furthermore, this occurs at a lower redshift, where the instrumental noise is expected to be lower. Naively, one would therefore expect astrophysical parameters to be more tightly constrained with a mock BRIGHT GALAXIES signal.

4 21 CM FORECASTS

We now quantify astrophysical parameter constraints for each of these two models, for both second-generation interferometers, HERA and SKA. We first summarize our 21CMMC configuration, and then provide parameter constraints while discussing their implications.

4.1 21CMMC set-up

As in Greig & Mesinger (2015), we use the 21 cm PS as the likelihood statistic to sample the astrophysical parameter space in 21CMMC. We adopt a modelling uncertainty of 20 per cent on the sampled 21 cm PS (not the mock observation of the 21 cm PS), which is added in quadrature with the total noise PS (equation 8).[18] As in Greig & Mesinger (2015), we compare the 21 cm PS at each redshift only over the reduced k-space range, $k = 0.15 - 1.0\,{\rm Mpc}^{-1}$, which we deem to be free of cosmic variance and shot-noise effects arising within the simulations.

We perform our forecasting using eight co-evolution[19] redshifts ($z = 6, 7, 8, 9, 11, 13, 15$ and 17). Note that our choice is relatively arbitrary, taken to span the EoH and EoR in both of our mock observations and is not driven by any computational or numerical reasons.

For the MCMC sampling, we use smaller boxes than used for the mock observations: 300^3 Mpc^3 volume on a 200^3 grid smoothed down from a high-resolution 1200^3 grid. Both the mock observations and the sampled 21 cm PS have the same voxel resolution ($\sim$1.5 Mpc per voxel). These box and cell sizes were selected to ensure per cent level convergence in the PS for a few randomly sampled astrophysical models.

Finally, it is instructive to provide some timing estimates for 21CMMC. We note that the public version of 21CMFAST is not optimized for our MCMC framework. Therefore, we heavily streamlined the computation for a single core implementation (since the advantage of 21CMMC is that a realization of 21CMFAST is performed for each available CPU core). For the 300^3 Mpc^3 volume, 200^3 voxel set-up above, our streamlined version of 21CMFAST is $\sim$20 $\times$ faster on a single core[20]. For our astrophysical parameter forecasting, we perform $\sim 8 \times 10^4$ 21CMFAST runs. As we are using the parallelized affine invariant ensemble sampler EMCEE, we can achieve $\sim 8 \times 10^4$ samplings with the following set-up: 400 walkers, each performed for 200 iterations[21]. Performed using 200 cores (i.e. 100 physical cores + 100 virtual cores) on a shared memory cluster, such a set-up takes $\sim$8 d.

4.2 Parameter recovery for the FAINT GALAXIES mock observation

In Fig. 3, we present the astrophysical parameter constraints for our FAINT GALAXIES model for our assumed 1000 h observation with both HERA (blue) and SKA (red). Across the diagonals, we provide the 1D marginalized probability distribution functions (PDFs) for each of the six model astrophysical parameters. In the lower left half of the figure, we provide the 2D marginalized joint likelihood contours, with crosses denoting the input fiducial values, while the thick and thin contours denote the 68 (1σ) and 95 (2σ) percentiles,

[18] A modelling uncertainty accounts for the inaccuracy of seminumerical approaches such as 21CMFAST. Here we simply take an uncorrelated fixed percentage error, with a value consistent with the comparisons in Zahn et al. (2011). This constant error purely accounts for the observed fractional differences in the recovered 21cm PS between the simulations. For example, it does not account for any potential errors arising from the different algorithms used to compute the IGM spin temperature. Future work will seek to characterize this uncertainty, potentially even mediating it by comparing 21CMFAST to suites of RT simulations.

[19] The observed 3D 21 cm signal is spatially dependent on the 2D sky, with the third (line-of-sight) direction being frequency dependent. The line-of-sight axis encodes evolution along the light-cone, which can impact the observed 21 cm PS, when compared to predictions from co-evolution cubes (e.g. Datta et al. 2012, 2014; La Plante et al. 2014; Ghara, Datta & Choudhury 2015). However, this effect is generally only pronounced on much larger scales than considered here (note that our lowest k-modes, $|k| = 0.15\,{\rm Mpc}^{-1}$, correspond to a modest $\Delta z \sim 0.1$ at EoR redshifts). We shall nevertheless return to this in future work, extending 21CMMC to operate directly on the light-cone.

[20] This boost in computational efficiency arises owing to the inclusion of additional interpolation tables to remove redundant calculations. Additionally, 21CMFAST is reduced to a single executable removing file I/O and limiting memory overheads.

[21] We explored several combinations of the walker/iterations configuration to confirm our experimental set-up was providing converged results for our MCMC.

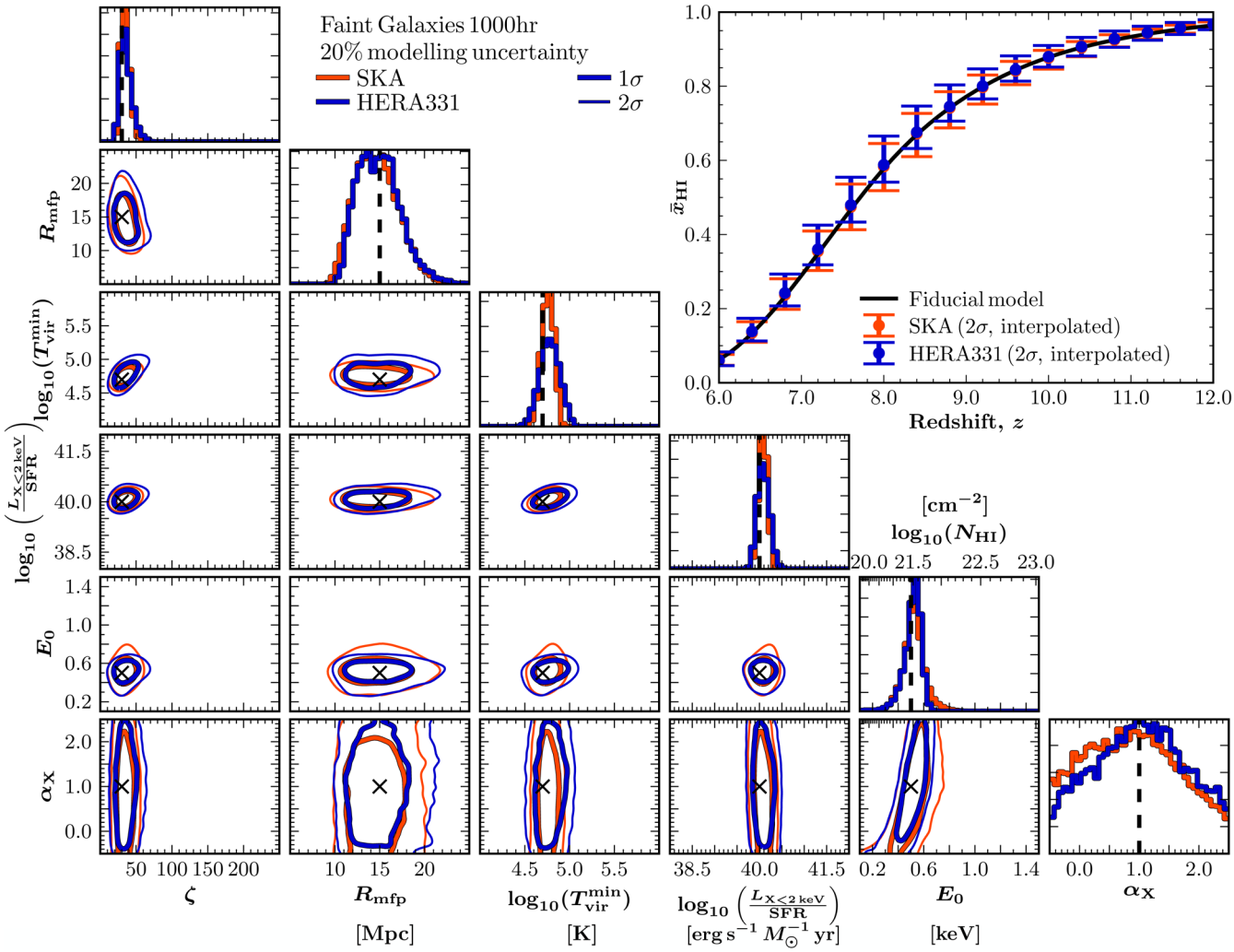

Figure 3. Recovered 1D and 2D marginalized joint posterior distributions for our FAINT GALAXIES six parameter astrophysical model for an assumed 1000 h on sky observation with HERA (blue) and SKA (red). Thick and thin contours correspond to the 68 (1σ) and 95 (2σ) per cent 2D marginalized joint likelihood constraints, respectively, and crosses (black vertical dashed lines) denote the input model parameters, defined to be (ζ, $R_{\rm mfp}$, $\log_{10}(T_{\rm vir}^{\rm min})$, $\log_{10}(L_{\rm X<2\,keV}/{\rm SFR})$, E_0, $\alpha_{\rm X}$) = (30, 15, 4.7, 40.0, 0.5, 1.0). Inset: The recovered global evolution of the IGM neutral fraction. The solid black curve corresponds to the fiducial input evolution, whereas the error bars correspond to the 2σ limits on the recovered IGM neutral fraction. Note, these points are interpolated at $\Delta z = 0.4$ purely for visualization.

respectively. In the top right half of the figure, we provide the 2σ marginalized constraints on the IGM neutral fraction, $\bar{x}_{\rm H\,I}$, with respect to the reionization history of the mock observation (solid black curve). Note that to generate this figure, we interpolate the reionization history between the marginalized distributions for $\bar{x}_{\rm H\,I}$ at the eight co-evolution redshifts, sampling at a rate of $\Delta z = 0.4$. In Table 3, we provide the median and associated 16th and 84th percentiles for each of our six astrophysical parameters for both HERA and SKA.

From the relatively narrow 1D PDFs, it is clear that both HERA and SKA can simultaneously constrain the EoR and EoH to high accuracy. The only parameter for which we do not achieve strong constraints is the X-ray spectral index, $\alpha_{\rm X}$. However, this is not overly surprising given the relatively small effect it has on the amplitude of the 21 cm PS over the entire allowed parameter range (see Fig. 1). Folding in the 20 per cent modelling uncertainty and the instrumental noise, the relative difference in the 21 cm PS amplitude across the full allowed parameter range is roughly consistent at about 2σ. In terms of the reionization history both HERA and SKA recover comparably tight constraints on the IGM neutral fraction. At 1σ, we recover constraints on $\bar{x}_{\rm H\,I}$ of the order of $\sim$5 per cent.

We recover no strong degeneracies with our astrophysical parameters, with mild degeneracies for ζ–$T_{\rm vir}^{\rm min}$, $L_{\rm X<2\,keV}/{\rm SFR}$–$T_{\rm vir}^{\rm min}$ and E_0–α_X. This is generally consistent with both Ewall-Wice et al. (2016) and Kern et al. (2017), whose mock observation most closely resembles our FAINT GALAXIES model. However, these authors find somewhat stronger $f_{\rm X}$–E_0 and $f_{\rm X}$–α_X degeneracies (where $f_{\rm X}$ corresponds to the number of X-ray photons per stellar baryon, and can thus be related to our $L_{\rm X<2\,keV}/{\rm SFR}$ for a given $\alpha_{\rm X}$ and E_0). This discrepancy could arise due to (i) the inclusion of the 20 per cent modelling uncertainty which broadens our contours; (ii) the approximations made in those works [assumptions of Gaussian errors in Fisher matrices (Ewall-Wice et al. 2016) or modelling errors in an emulator method Kern et al. (2017)]; and/or (iii) our choice for the soft-band *energy* as a normalization parameter (instead of

Table 3. Summary of the median recovered values (and associated 16th and 84th percentiles errors) for the six-parameter astrophysical model describing the EoR and EoH, ζ, $R_{\rm mfp}$, $\log_{10}(T_{\rm vir}^{\rm min})$, $\log_{10}(L_{X<2\,{\rm keV}}/{\rm SFR})$, E_0 and α_X. We assume a total 1000 h integration time with both the SKA and HERA. Our fiducial mock observation, corresponding to the FAINT GALAXIES model, assumes (ζ, $R_{\rm mfp}$, $\log_{10}(T_{\rm vir}^{\rm min})$, $\log_{10}(L_{X<2\,{\rm keV}}/{\rm SFR})$, E_0, α_X) = (30, 15, 4.7, 40.0, 0.5, 1.0). We also provide the recovered biased constraints when we ignore the IGM spin temperature fluctuations (i.e. $T_S \gg T_{\rm CMB}$; see Section 5.1).

FAINT GALAXIES Model/instrument	Parameter ζ	$R_{\rm mfp}$ (Mpc)	$\log_{10}(T_{\rm vir}^{\rm min})$ (K)	$\log_{10}(L_{X<2\,{\rm keV}}/{\rm SFR})$ (erg s^{-1} M$_\odot^{-1}$ yr)	E_0 (keV)	α_X
Full X-ray heating						
HERA 331	$34.69^{+9.48}_{-6.50}$	$14.82^{+2.47}_{-2.29}$	$4.78^{+0.11}_{-0.11}$	$40.08^{+0.14}_{-0.12}$	$0.52^{+0.08}_{-0.05}$	$1.01^{+0.82}_{-0.85}$
SKA	$33.99^{+7.18}_{-5.13}$	$14.56^{+2.58}_{-2.29}$	$4.76^{+0.07}_{-0.07}$	$40.08^{+0.10}_{-0.10}$	$0.52^{+0.07}_{-0.08}$	$0.87^{+0.86}_{-0.85}$
Ignoring T_S ($T_S \gg T_{\rm CMB}$)						
HERA 331	$18.98^{+7.81}_{-2.80}$	$16.80^{+3.36}_{-2.67}$	$4.44^{+0.24}_{-0.13}$	–	–	–
SKA	$15.51^{+4.97}_{-2.20}$	$16.99^{+3.75}_{-4.17}$	$4.29^{+0.17}_{-0.11}$	–	–	–

the X-ray photon *number*), which can provide a more independent basis vector for the EoH evolution.[22]

If we assume that the 1D marginalized PDFs can be modelled by a normal distribution, which for the most part is reasonable at the 1σ level (i.e. some tails begin to appear at $\sim 2\sigma$), we can provide some approximate fractional uncertainties for the astrophysical parameters. For the SKA (HERA), the 1σ percentage errors are: $\zeta = 18$ (24), $R_{\rm mfp} = 16$ (16), $\log_{10}(T_{\rm vir}^{\rm min}) = 1.4$ (2.3), $\log_{10}(L_{X<2\,{\rm keV}}/{\rm SFR}) = 0.2$ (0.3), $E_0 = 17$ (14) and $\alpha_X = 88$ (73). The uncertainty on the EoR parameters is comparable to what we obtained in Greig & Mesinger (2015): $\zeta = 17$ (22), $R_{\rm mfp} = 18$ (18), $\log_{10}(T_{\rm vir}^{\rm min}) = 2.4$ (3.3). Therefore, despite increasing the model complexity by including the EoH, the relative constraints are comparable.

Ewall-Wice et al. (2016) quote fractional precisions on their six-parameter model, with 1–2 per cent accuracy on the EoR parameters and 6 per cent on their EoH parameters. Their constraints are smaller than ours by about an order of magnitude for the EoR and factor of a few for the EoH. Approximately half of this difference can be attributed to the inclusion of the modelling uncertainty (see e.g. Greig & Mesinger 2015). The remaining discrepancy can arise from either the fundamental assumptions in their Fisher matrix approach, or their larger number of redshift samples (more than a factor of 2). In future, we will modify 21CMMC to directly work on the observed light-cone, removing the necessity of an ad hoc sampling of co-evolution cubes.

For our FAINT GALAXIES model, we find both HERA and SKA will recover comparable parameter constraints. This is despite the significantly increased sensitivity achievable with the SKA, resulting in a larger total integrated signal to noise (S/N). As pointed out in Greig & Mesinger (2015), the S/N is not a reliable metric for predicting an instrument's ability at parameter constraints, since model constraining power is biased towards large scales. This highlights the importance of using parameter forecasting as a figure of merit, instead of just the total S/N. We caution however that the SKA performance can be improved if one can better mediate modelling uncertainties. Indeed, the increased thermal noise sensitivity on small scales is washed out by our assumed 20 per cent modelling uncertainty. Moreover, the SKA will be superior at tomography; using higher order likelihood statistics should therefore favour the SKA over HERA.

[22] In selecting the soft-band X-ray luminosity instead of a harder X-ray band (e.g. 0.5–8 keV), we have preferentially minimized the degeneracy between the X-ray luminosity and α_X. Additionally, adopting a soft-band X-ray luminosity enables straightforward comparison with numerous observations of nearby galaxies (e.g. Tzanavaris & Georgantopoulos 2008; Mineo, Gilfanov & Sunyaev 2012b; Fragos et al. 2013b; Lehmer et al. 2015, 2016). In the near future, we expect observations of the intrinsic soft-band X-ray luminosity escaping the host galaxy to improve the upcoming Athena telescope (Barcons et al. 2012), which will provide a soft-band effective area more than an order of magnitude larger than existing experiments (T. Dauser, private communication). This will provide stronger priors on the X-ray SED, even if 21 cm observations themselves are less discriminatory.

4.3 Parameter recovery for the BRIGHT GALAXIES mock observation

In Fig. 4, we present our 1D and 2D joint marginalized posterior distributions for each of the six astrophysical parameters for our BRIGHT GALAXIES model assuming a 1000 h observation with HERA (blue) and the SKA (red). Table 4 provides the median and associated 16th and 84th percentiles for each of our astrophysical model parameters. As in the previous section, we provide approximate fractional precisions on the model parameters assuming normally distributed marginal likelihoods. For the SKA (HERA), the 1σ percent errors are: $\zeta = 17$ (15), $R_{\rm mfp} = 16$ (12), $\log_{10}(T_{\rm vir}^{\rm min}) = 0.4$ (0.6), $\log_{10}(L_{X<2\,{\rm keV}}/{\rm SFR}) = 0.2$ (0.2), $E_0 = 16$ (17) and $\alpha_X = 80$ (79).

The constraints are comparable for most of the astrophysical parameters held fixed across the two models (i.e. $R_{\rm mfp}$, $\log_{10}(L_{X<2\,{\rm keV}}/{\rm SFR})$, E_0, α_X). The largest difference is in $R_{\rm mfp}$, which shows tighter constraints relative to the FAINT GALAXIES model. At a given stage in the EoR, the H II regions in the BRIGHT GALAXIES model are larger and more isolated, sourced by the brighter, rarer, more-biased sources. Recombinations play a larger role in limiting the growth of such H II regions, whose characteristic sizes approach $R_{\rm mfp}$ earlier in reionization. Since the signal is more sensitive to $R_{\rm mfp}$, a degeneracy between ζ and $R_{\rm mfp}$ emerges, with both now able to control the timing of the EoR: one can compensate for the slowing-down of the EoR due to recombinations (a smaller $R_{\rm mfp}$) by increasing the ionizing efficiency, ζ. This degeneracy leads to poorer overall constraints on ζ when compared to the FAINT GALAXIES model.

These improvements in the constraints of $R_{\rm mfp}$ are however only available with HERA. The marginalized PDFs for the SKA exhibit a noticeable tail towards increasing $R_{\rm mfp}$. The source of this tail can simply be attributed to the reduced large-scale sensitivity of the SKA relative to HERA owing to our adopted observing strategies within this work (see Section 2.3 and Fig. A2).

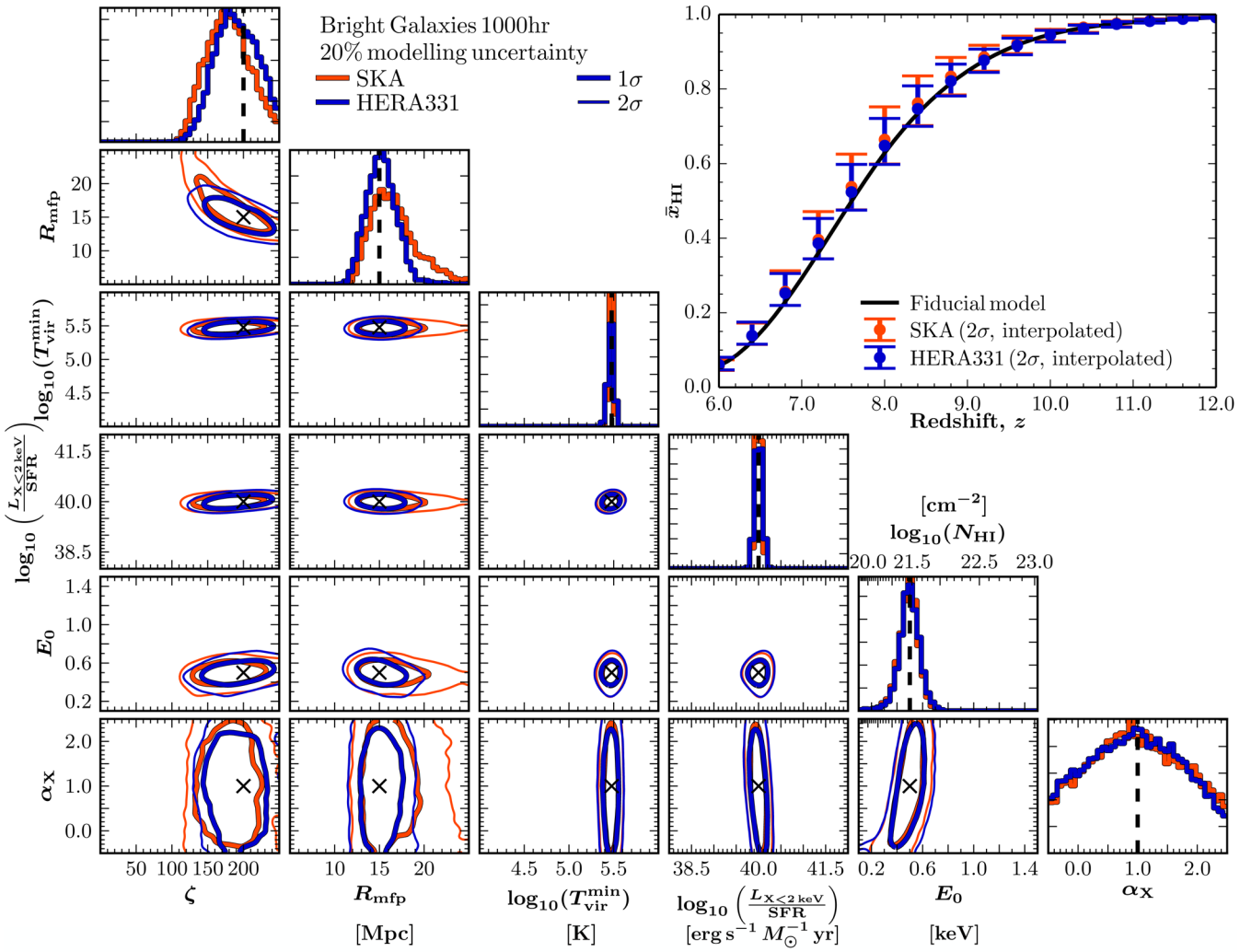

Figure 4. The same as Fig. 3 except for the BRIGHT GALAXIES model. Crosses (black vertical dashed lines) denote the input model parameters, defined to be (ζ, $R_{\rm mfp}$, $\log_{10}(T_{\rm vir}^{\rm min})$, $\log_{10}(L_{X<2\,{\rm keV}}/{\rm SFR})$, E_0, α_X) = (200, 15, 5.48, 40.0, 0.5, 1.0).

Table 4. The same as Table 3 except now for the BRIGHT GALAXIES model. Our BRIGHT GALAXIES mock observation assumes (ζ, $R_{\rm mfp}$, $\log_{10}(T_{\rm vir}^{\rm min})$, $\log_{10}(L_{X<2\,{\rm keV}}/{\rm SFR})$, E_0, α_X) = (200, 15, 5.48, 40.0, 0.5, 1.0).

BRIGHT GALAXIES	Parameter					
Model/instrument	ζ	$R_{\rm mfp}$ (Mpc)	$\log_{10}(T_{\rm vir}^{\rm min})$ (K)	$\log_{10}(L_{X<2\,{\rm keV}}/{\rm SFR})$ (erg s^{-1} M$_\odot^{-1}$ yr)	E_0 (keV)	α_X
Full X-ray heating						
HERA 331	$188.59^{+32.66}_{-29.73}$	$15.21^{+1.75}_{-1.65}$	$5.47^{+0.03}_{-0.03}$	$40.00^{+0.08}_{-0.08}$	$0.50^{+0.08}_{-0.07}$	$0.95^{+0.84}_{-0.86}$
SKA	$177.32^{+33.62}_{-30.85}$	$16.33^{+2.91}_{-2.08}$	$5.47^{+0.02}_{-0.02}$	$40.00^{+0.07}_{-0.07}$	$0.50^{+0.07}_{-0.08}$	$0.95^{+0.91}_{-0.82}$
Ignoring T_S ($T_S \gg T_{\rm CMB}$)						
HERA 331	$25.50^{+12.42}_{-4.68}$	$13.15^{+1.25}_{-1.19}$	$4.55^{+0.22}_{-0.13}$	–	–	–
SKA	$15.65^{+3.47}_{-2.22}$	$11.17^{+2.06}_{-1.67}$	$4.18^{+0.13}_{-0.11}$	–	–	–

5 CAN WE IGNORE THE SPIN TEMPERATURE IN EOR PARAMETER RECOVERY?

The majority of studies that constrain the EoR with the cosmic 21 cm signal assume that the IGM spin temperature is saturated (i.e. $T_S \gg T_{\rm CMB}$). Since the corresponding term in the brightness temperature saturates to unity in this regime (cf. equation 1), assuming saturation greatly simplifies the computational load. However, the validity of such an approximation is highly dependent on the poorly constrained relative efficiencies of ionizing and

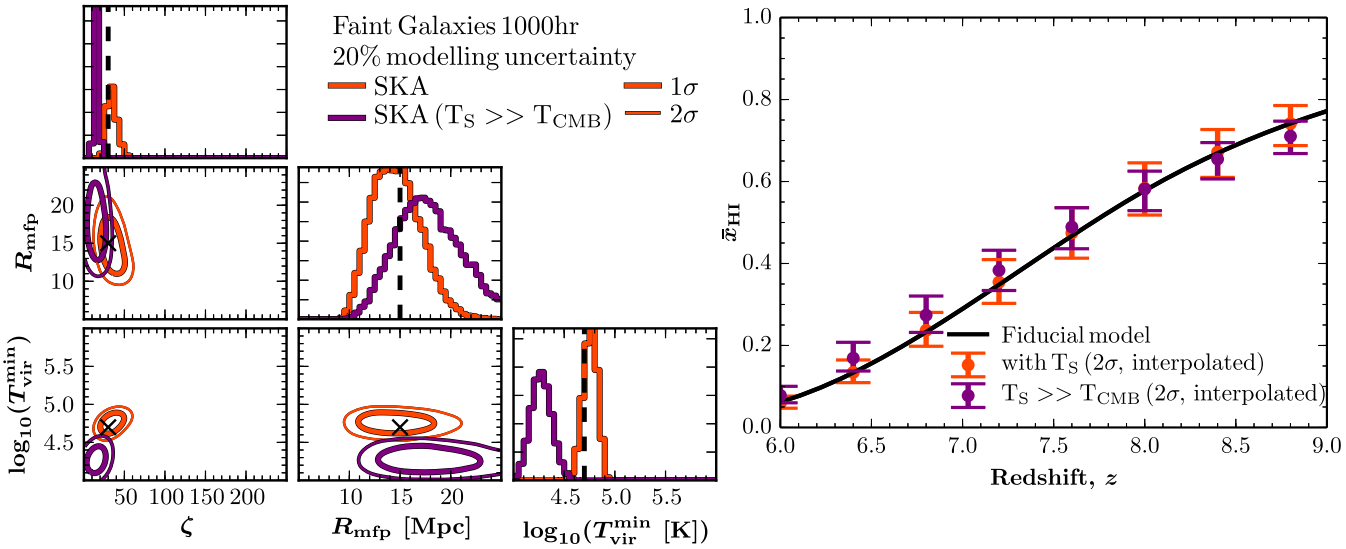

Figure 5. The impact of the common saturated spin temperature approximation ($T_S \gg T_{CMB}$) on EoR parameter inference. We show the recovered 1D and 2D joint marginalized posterior distributions for the FAINT GALAXIES model assuming a 1000 h on sky observation with the SKA. Red curves correspond to our fiducial constraints which include the spin temperature modelling (marginalizing over the EoH parameter) accounting for the IGM spin temperature fluctuations (Fig. 3), whereas the purple curves are the recovered constraints when ignoring the IGM spin temperature fluctuations (i.e. $T_S \gg T_{CMB}$). Thick and thin contours correspond to the 68 (1σ) and 95 (2σ) per cent marginalized joint likelihood contours, respectively, and crosses (black vertical dashed lines) denote the input model parameters, defined to be $(\zeta, R_{mfp}, \log_{10}(T_{vir}^{min})) = (30, 15, 4.7)$. Inset: The recovered global evolution of the IGM neutral fraction. The solid black curve corresponds to the fiducial input evolution, whereas the error bars correspond to the 2σ limits on the recovered IGM neutral fraction. Note, all points are interpolated at $\Delta z = 0.4$ purely for visualization purposes only.

X-ray sources in the first galaxies. Not properly taking into account the IGM spin temperature can bias the recovered EoR parameter constraints.[23] Here, we quantify the impact of this using our two mock 21 cm observations. The two adopted extrema in T_{vir}^{min} allow the exploration of vastly different levels of overlap between the EoR and EoH, enabling us to estimate the available span in the corresponding bias. Here, we use 21CMMC to recover the fractional precision on the EoR parameters under the simplification of $T_S \gg T_{CMB}$, and compare these to the constraints obtained by properly modelling T_S.

5.1 FAINT GALAXIES

The 21 cm signal for the FAINT GALAXIES model transitions from absorption to emission at $z \lesssim 12$ (see e.g. the middle panel of Fig. 2). At lower redshifts, the IGM spin temperature continues to increase and the $(1 - T_{CMB}/T_S)$ factor approaches unity. Assuming the saturated limit ($T_S \gg T_{CMB}$) results in a fractional error in the PS less than 10 per cent when $(1 - T_{CMB}/T_S)^2 \gtrsim 0.9$, corresponding to $z \sim 7.3$ and an IGM neutral fraction of $\bar{x}_{H\,I} \sim 0.4$ (cf. the similar FAINT GALAXIES model considered in Mesinger et al. 2016). Therefore, the saturated spin temperature approximation is only reasonable during the second half of reionization in our FAINT GALAXIES model.

[23] In Ewall-Wice et al. (2016), these authors found that by incorrectly accounting for the EoH, their recovered uncertainties in the EoR parameters could be biased. They explored this by fitting their EoR parameters by either (i) assuming a fixed EoH model; or (ii) properly fitting and marginalizing over the EoH model parameters. The fractional uncertainties from (i) were smaller than (ii) by almost a factor of 2. This emphasizes the importance of properly accounting for the EoH when performing astrophysical parameter recovery from the 21 cm signal.

In Fig. 5, we present the 1D and 2D joint marginalized posterior distributions for the EoR parameters, namely ζ, R_{mfp} and $\log_{10}(T_{vir}^{min})$. For this comparison, we only consider the SKA (the results for HERA are nearly identical as shown in Table 3), and run 21CMMC on the redshifts spanning the EoR: $z = 6, 7, 8$ and 9. Red curves correspond to the constraints on the EoR model parameters from fitting the full six parameter astrophysical model (i.e. including the EoH, Fig. 3), whereas the purple curves correspond to the constraints obtained with the saturated spin temperature approximation. In the lower half of Table 3, we provide the median, 16th and 84th percentiles for the recoverer uncertainties on the EoR parameters.

It is clear from Fig. 5 that the saturated spin temperature approximation significantly biases parameter constraints. The saturated temperature approximation prefers models with a smaller virial temperature and ionizing efficiency compared to the 'true' ones. The marginalized 1D PDFs for T_{vir}^{min} are offset by at least $\sim 3\sigma$. For ζ, we recover more modest offsets of $\sim 1.5\sigma$, and for R_{mfp} we recover comparable constraints. In all cases, the recovered astrophysical constraints return larger uncertainties, owing to the lower marginalized likelihoods. For reference, the maximum likelihood (ML: $\mathcal{L} = \exp(-\frac{1}{2}\chi^2)$) is a factor of 4 lower than obtained with the full spin temperature modelling in Section 4.2.

To understand this bias, in Fig. 6 we show the 21 cm PS for the mock observation (black curve), the ML 21 cm PS assuming $T_S \gg T_{CMB}$ (red curve) and the 21 cm PS adopting the 'true' EoR model parameters assuming $T_S \gg T_{CMB}$ (blue curve). Error bars denote the 20 per cent modelling uncertainty on the model 21 cm PS. The main impact of ignoring the spin temperature can be seen by comparing the blue and black curves. Since both curves are generated from the same EoR model parameters, any discrepancies arise from the spin temperature. The largest discrepancy, as expected, arises at the highest redshift, where the IGM is still undergoing the final stages

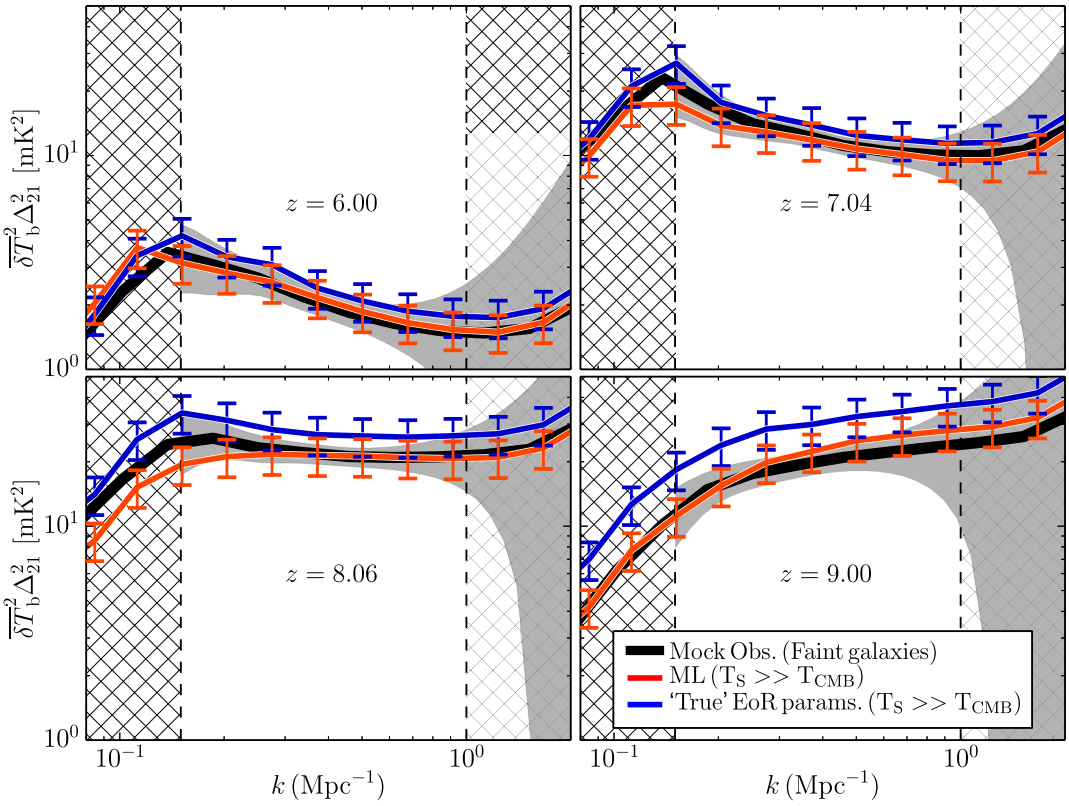

Figure 6. The 21 cm PS corresponding to the maximum likelihood model assuming a saturated spin temperature ($T_S \gg T_{CMB}$; red curve), compared to the fiducial mock 21 cm PS of the FAINT GALAXIES model (black curve). The blue curve corresponds to the 'true' EoR model parameters, $(\zeta, R_{mfp}, \log_{10}(T_{vir}^{min})) = (30, 15, 4.7)$, but is computed assuming a saturated spin temperature. The grey shaded region corresponds to the 1σ observational uncertainty for an assumed 1000 h observation with the SKA, while the error bars denote our assumed 20 per cent modelling uncertainty on the 21 cm PS. Hatched regions denote k-modes outside of our nominal fitting range.

of X-ray heating. As discussed in Mesinger et al. (2016), during the EoR the cosmic H I patches effectively have the same, uniform IGM spin temperature, resulting in fairly negligible temperature fluctuations for the FAINT GALAXIES model (see also Pober et al. 2015). However, the amplitude of the 21 cm PS is decreased by a factor of $(1 - T_{CMB}/T_S)^2$ (compare the blue and black curves at $z \sim 8$–9). In order to mimic this $(1 - T_{CMB}/T_S)^2$ decrease in amplitude, a model that assumes $T_S \gg T_{CMB}$ will tend to prefer EoR models with intrinsically less power, i.e. those in which the sources are less biased, having a lower T_{vir}^{min}. A lower T_{vir}^{min} implies more abundant ionizing sources, which must be compensated for by decreasing ζ to attempt to recover the correct reionization history. Therefore, the likelihood peaks at smaller virial temperatures and ionizing efficiencies (cf. the red curve, corresponding to $T_{vir}^{min} = 10^{4.29}$ K and $\zeta = 15.5$). The full evolution of the PS is unable to be completely reproduced, producing the factor of 4 lower ML compared to the complete model including the EoH[24].

5.2 BRIGHT GALAXIES

Already for the FAINT GALAXIES model, we find significant biases in the recovered EoR parameters under the assumption that the spin temperature is saturated. In the BRIGHT GALAXIES model, the EoH and EoR overlap even more strongly, in effect maximizing this bias in parameter recovery. We quantify this in Fig. 7, in which we provide the marginalized distributions, and in the lower half of Table 4 where we provide the median, 16th and 84th percentiles for our recovered EoR model parameters.

For both ζ and T_{vir}^{min}, we recover marginalized constraints discrepant at $>10\sigma$. As in the FAINT GALAXIES model, R_{mfp} remains consistent to within 1σ, but it instead prefers marginally lower values, $R_{mfp} \sim 10$ Mpc. In the inset of Fig. 7, the recovered reionization history is discrepant at the $>5\sigma$ level, beyond $z \sim 7.5$. In Fig. 8, we present the 21 cm PS from the mock BRIGHT GALAXIES model, the ML estimate and the 'true' EoR model parameters assuming the saturated spin temperature limit. It is immediately evident that all the constraining power for the ML arises from the 21 cm PS at $z = 6$ and 7. At $z > 7$, the saturated limit cannot reproduce the reduced amplitude of the mock 21 cm PS.[25]

This is not surprising. As discussed in Section 4.3, the global averaged 21 cm brightness temperature contrast is still in absorption at $z > 8$ (see Fig. 2), indicating $T_S \lesssim T_{CMB}$ for a significant fraction of the simulation volume. At the same time, the IGM is 35 per cent ionized ($\bar{x}_{H\,I} = 0.65$) by $z = 8$, indicating reionization is well underway. This significant overlap of the EoR and EoH breaks the fundamental assumption of the saturated spin temperature limit. Furthermore, at $z = 8$ the BRIGHT GALAXIES model is transitioning closely to the $T_S \equiv T_{CMB}$ limit, producing a precipitous drop in the 21 cm PS amplitude. Relative to the BRIGHT

[24] Note, that the ML from our six-parameter model was computed from eight different redshifts, whereas in the saturated limit we only considered four redshifts. As additional redshift data decreases the unnormalized ML value of a model, the relative differences here are even larger.

[25] For reference, the ML is $\sim 10^{28}$ times lower when we assume $T_S \gg T_{CMB}$.

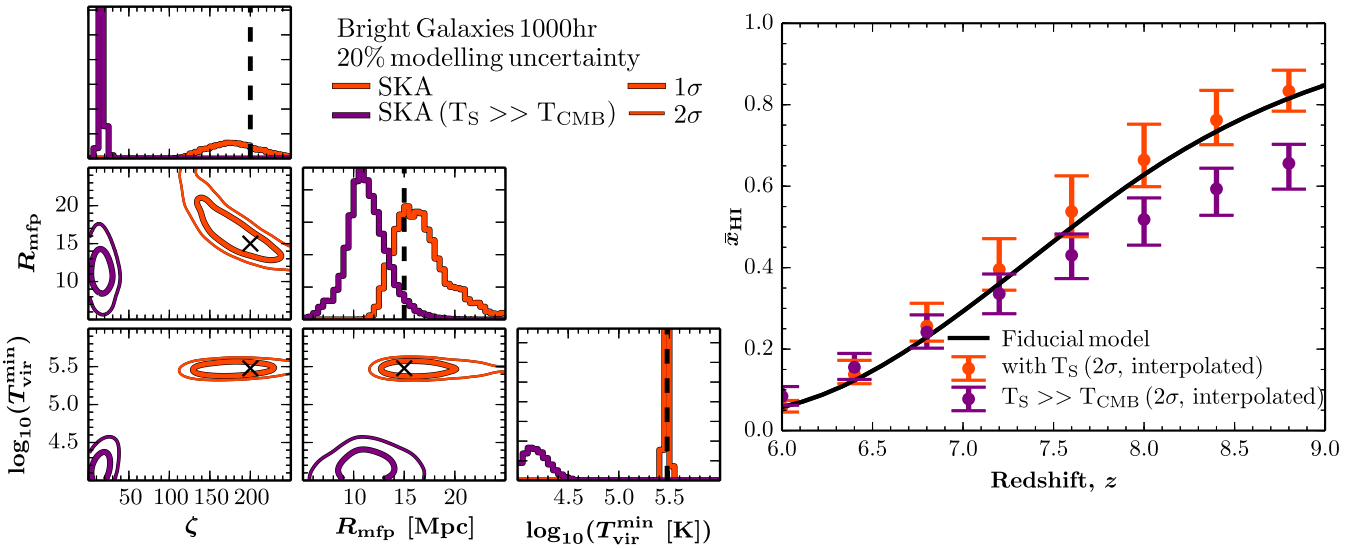

Figure 7. The same as Fig. 5, except for our BRIGHT GALAXIES model. Crosses (black vertical dashed lines) denote the input model parameters, defined to be $(\zeta, R_{\rm mfp}, \log_{10}(T_{\rm vir}^{\rm min})) = (200, 15, 5.48)$.

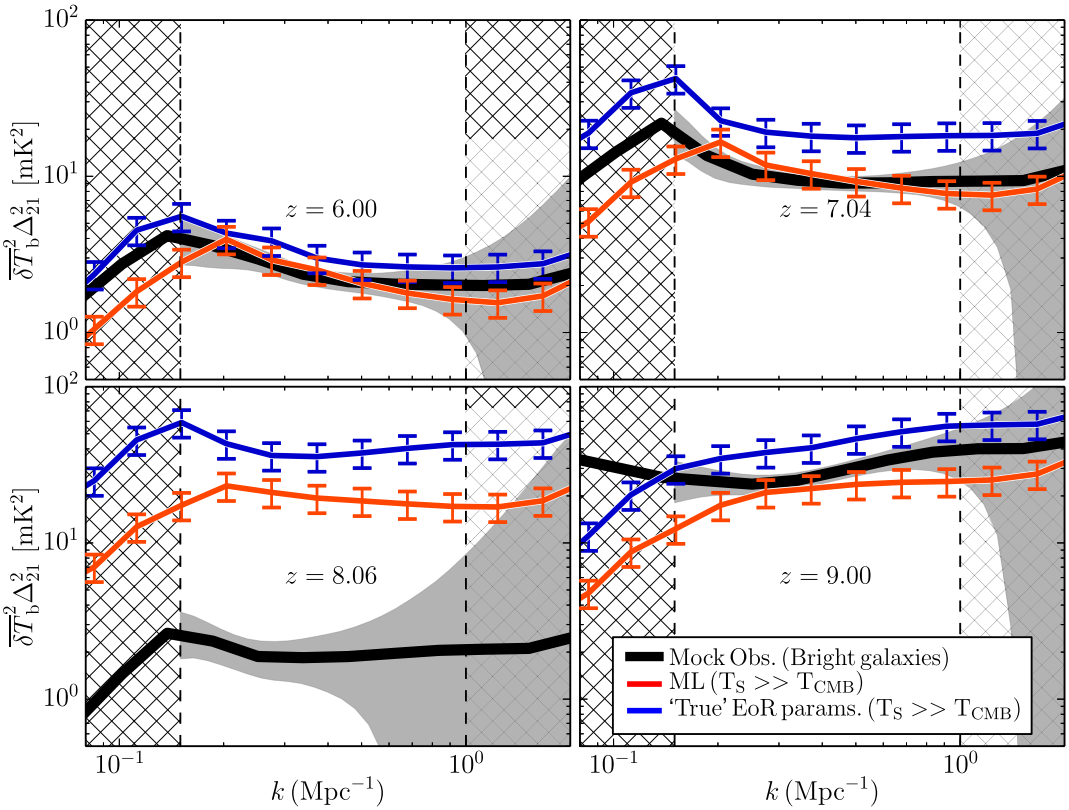

Figure 8. The same as Fig. 6, except for our BRIGHT GALAXIES model. The fiducial BRIGHT GALAXIES EoR parameter set corresponds to $(\zeta, R_{\rm mfp}, \log_{10}(T_{\rm vir}^{\rm min})) = (200, 15, 5.48)$.

GALAXIES model in the saturated limit (blue curve), this is a factor of ∼40 difference in the 21 cm PS amplitude. Under the saturated limit assumption, there is no avenue to mimic such behaviour, resulting in hugely discrepant astrophysical parameter constraints.

This highlights the importance of properly including the EoH. Incorrectly ignoring the EoH and associated IGM spin temperature fluctuations when interpreting a realistic observation could significantly bias the inferred EoR source model.

6 CONCLUSION

Detecting the cosmic 21 cm signal during the EoR and the EoH stands to reveal insights into the formation, growth and evolution of

structure in the Universe. However, how do we interpret the underlying astrophysics once we have a detection? To aid this, we developed 21CMMC, a massively parallel Bayesian MCMC analysis tool, which performs full 3D reionization simulations (using 21CMFAST) on the fly, for recovering EoR astrophysical parameter constraints. Second-generation experiments such as HERA and the SKA, along with global 21 cm experiments, will be able to measure both the EoR and the pre-heating of the IGM by X-rays. Therefore, in order to facilitate simultaneous astrophysical forecasting of the EoR and EoH and consequently aid in the development and construction of the data reduction and signal extraction pipelines, in this work we extend 21CMMC into the epoch of X-ray heating.

We demonstrate that both HERA and the SKA will be able to simultaneously constrain the astrophysics of reionization and the X-ray heating. We consider two models describing the mock observation: FAINT GALAXIES and BRIGHT GALAXIES. These are intended to encompass the physically plausible region of parameter space provided by extrapolating the faint end of the observed UV luminosity function.

Assuming a 1000 h observation of the 21 cm PS at eight co-evolution redshifts, we recover the fractional precision on our six-parameter model describing the sources responsible for the EoR and the EoH. These parameters include an ionizing source efficiency (ζ), effective photon horizon ($R_{\rm mfp}$), minimum halo mass of ionizing sources ($T_{\rm vir}^{\rm min}$), soft-band luminosity (<2 keV) of X-ray sources ($L_{\rm X<2keV}/{\rm SFR}$), minimum energy threshold for the attenuation of the X-rays by the host galaxy ISM (E_0) and the spectral index of the X-ray source SED ($\alpha_{\rm X}$). Additionally assuming a 20 per cent modelling uncertainty in the PS, we recover the parameters of the mock signals with the following percentage error (1σ):

(i) FAINT GALAXIES: $\zeta = 18$ (24), $R_{\rm mfp} = 16$ (16), $\log_{10}(T_{\rm vir}^{\rm min}) = 1.4$ (2.3), $\log_{10}(L_{\rm X<2keV}/{\rm SFR}) = 0.2$ (0.3), $E_0 = 17$ (14) and $\alpha_{\rm X} = 88$ (73), respectively, for the SKA (HERA).

(ii) BRIGHT GALAXIES: $\zeta = 17$ (15), $R_{\rm mfp} = 16$ (12), $\log_{10}(T_{\rm vir}^{\rm min}) = 0.4$ (0.6), $\log_{10}(L_{\rm X<2keV}/{\rm SFR}) = 0.2$ (0.2), $E_0 = 16$ (17) and $\alpha_{\rm X} = 80$ (79), respectively, for the SKA (HERA).

Both the SKA and HERA perform equally as well at simultaneously constraining the astrophysics of reionization and the epoch of X-ray heating due to their comparable sensitivities on the large scales (under our assumptions regarding the survey strategy) which most strongly discriminate between the astrophysical models.

With our expanded framework, we also quantify the impact of the common assumption of a saturated spin temperature, $T_{\rm S} \gg T_{\rm CMB}$, during the EoR. Our FAINT GALAXIES model has a relatively distinct EoH and EoR, for which we would typically expect $T_{\rm S} \gg T_{\rm CMB}$ to be a reasonable approximation during the bulk of reionization. Nevertheless, even this modest overlap of epochs leads to biases in ζ and $T_{\rm vir}^{\rm min}$ of up to $\sim 3\sigma$, and a reduction in the ML by a factor of >4. The BRIGHT GALAXIES model on the other hand represents the extreme case of EoR and EoH overlap. For this model, the recovered constraints are discrepant at $>10\sigma$, with the ML under in the saturated limit being a factor of $\sim 10^{28}$ lower than in the full model. Therefore, adopting the saturated spin temperature approximation can significantly bias inferences on EoR parameters.

ACKNOWLEDGEMENTS

We thank Adrian Liu and Nicholas Kern for comments on a draft version of this work. This work was supported by the European Research Council (ERC) under the European Union's Horizon 2020 research and innovation programme (grant agreement No 638809 – AIDA – PI: Mesinger).

REFERENCES

Abel T., Bryan G. L., Norman M. L., 2002, Science, 295, 93
Akeret J., Seehars S., Amara A., Refregier A., Csillaghy A., 2013, Astron. Comput., 2, 27
Ali Z. S. et al., 2015, ApJ, 809, 61
Alvarez M. A., Abel T., 2012, ApJ, 747, 126
Baek S., Semelin B., Matteo P. D., Revaz Y., Combes F., 2010, A&A, 523, A4
Barcons X. et al., 2012, preprint (arXiv:1207.2745)
Barkana R., Loeb A., 2001, Phys. Rep., 349, 125
Barkana R., Loeb A., 2005, ApJ, 626, 1
Barkana R., Loeb A., 2007, Rep. Prog. Phys., 70, 627
Barone-Nugent R. L. et al., 2014, ApJ, 793, 17
Beardsley A., Morales M., Lidz A., Malloy M., Sutter P., 2015, ApJ, 800, 128
Behroozi P. S., Silk J., 2015, ApJ, 799, 32
Bernardi G. et al., 2016, MNRAS, 461, 2847
Bolton J. S., Haehnelt M. G., 2007, MNRAS, 382, 325
Bond J. R., Cole S., Efstathiou G., Kaiser N., 1991, ApJ, 379, 440
Bouwens R. J. et al., 2015, ApJ, 803, 34
Bowman J. D., Rogers A. E. E., 2010, Nature, 468, 796
Bromm V., Coppi P. S., Larson R. B., 2002, ApJ, 564, 23
Burns J. O. et al., 2012, Adv. Space Res., 49, 433
Cirelli M., Iocco F., Panci P., 2009, J. Cosmol. Astropart. Phys., 10, 009
Das A., Mesinger A., Pallottini A., Ferrara A., Wise J. H., 2017, MNRAS, 469, 1166
Datta A., Bowman J. D., Carilli C. L., 2010, ApJ, 724, 526
Datta K. K., Mellema G., Mao Y., Iliev I. T., Shapiro P. R., Ahn K., 2012, MNRAS, 424, 1877
Datta K. K., Jensen H., Majumdar S., Mellema G., Iliev I. T., Mao Y., Shapiro P. R., Ahn K., 2014, MNRAS, 442, 1491
DeBoer D. R. et al., 2017, PASP, 129, 045001
Dijkstra M., Gilfanov M., Loeb A., Sunyaev R., 2012, MNRAS, 421, 213
Evoli C., Mesinger A., Ferrara A., 2014, J. Cosmol. Astropart. Phys., 11, 024
Ewall-Wice A., Hewitt J., Mesinger A., Dillon J. S., Liu A., Pober J., 2016, MNRAS, 458, 2710
Fialkov A., Barkana R., Visbal E., Tseliakhovich D., Hirata C. M., 2013, MNRAS, 432, 2909
Fialkov A., Barkana R., Visbal E., 2014, Nature, 506, 197
Fialkov A., Cohen A., Barkana R., Silk J., 2017, MNRAS, 464, 3498
Field G. B., 1958, Proc. Inst. Radio Eng., 46, 240
Foreman-Mackey D., Hogg D. W., Lang D., Goodman J., 2013, PASP, 125, 306
Fragos T. et al., 2013a, ApJ, 764, 41
Fragos T., Lehmer B. D., Naoz S., Zezas A., Basu-Zych A., 2013b, ApJ, 776, L31
Furlanetto S. R., 2006, MNRAS, 371, 867
Furlanetto S. R., Mesinger A., 2009, MNRAS, 394, 1667
Furlanetto S. R., Oh S. P., 2005, MNRAS, 363, 1031
Furlanetto S. R., Zaldarriaga M., Hernquist L., 2004, ApJ, 613, 1
Furlanetto S. R., Oh S. P., Briggs F. H., 2006, Phys. Rep., 433, 181
Ghara R., Datta K. K., Choudhury T. R., 2015, MNRAS, 453, 3143
Ghara R., Choudhury T. R., Datta K. K., 2016, MNRAS, 460, 827
Gnedin N. Y., Ostriker J. P., 1997, ApJ, 486, 581
Gnedin N. Y., Shaver P. A., 2004, ApJ, 608, 611
Goodman J., Weare J., 2010, Commun. Appl. Math. Comput. Sci., 5, 1
Greenhill L. J., Bernardi G., 2012, preprint (arXiv:1201.1700)
Greig B., Mesinger A., 2015, MNRAS, 449, 4246
Greig B., Mesinger A., Koopmans L. V. E., 2015, preprint (arXiv:1509.03312)
Haiman Z., Bryan G. L., 2006, ApJ, 650, 7
Haiman Z., Thoul A. A., Loeb A., 1996, ApJ, 464, 523
Haiman Z., Abel T., Rees M. J., 2000, ApJ, 534, 11
Hazelton B. J., Morales M. F., Sullivan I. S., 2013, ApJ, 770, 156
Holzbauer L. N., Furlanetto S. R., 2012, MNRAS, 419, 718
Kern N. S., Liu A., Parsons A. R., Mesinger A., Greig B., 2017, preprint (arXiv:1705.04688)

Kimm T., Katz H., Haehnelt M., Rosdahl J., Devriendt J., Slyz A., 2017, MNRAS, 466, 4826
Kuhlen M., Faucher-Giguère C.-A., 2012, MNRAS, 423, 862
La Plante P., Battaglia N., Natarajan A., Peterson J. B., Trac H., Cen R., Loeb A., 2014, ApJ, 789, 31
Lacey C., Cole S., 1993, MNRAS, 262, 627
Lehmer B. D. et al., 2012, ApJ, 752, 46
Lehmer B. D. et al., 2013, ApJ, 771, 134
Lehmer B. D. et al., 2015, ApJ, 806, 126
Lehmer B. D. et al., 2016, ApJ, 825, 7
Leite N., Evoli C., D'Angelo M., Ciardi B., Sigl G., Ferrara A., 2017, MNRAS, 469, 416
Lidz A., Zahn O., McQuinn M., Zaldarriaga M., Dutta S., Hernquist L., 2007, ApJ, 659, 865
Lidz A., Zahn O., McQuinn M., Zaldarriaga M., Hernquist L., 2008, ApJ, 680, 962
Liu A., Parsons A. R., Trott C. M., 2014a, Phys. Rev. D, 90, 023018
Liu A., Parsons A. R., Trott C. M., 2014b, Phys. Rev. D, 90, 023019
Loeb A., Furlanetto S. R., 2013, The First Galaxies in the Universe. Princeton Univ. Press, Princeton, NJ
Lopez-Honorez L., Mena O., Moliné Á., Palomares-Ruiz S., Vincent A. C., 2016, J. Cosmol. Astropart. Phys., 08, 004
McQuinn M., 2012, MNRAS, 426, 1349
McQuinn M., O'Leary R. M., 2012, ApJ, 760, 3
McQuinn M., Zahn O., Zaldarriaga M., Hernquist L., Furlanetto S. R., 2006, ApJ, 653, 815
McQuinn M., Lidz A., Zahn O., Dutta S., Hernquist L., Zaldarriaga M., 2007, MNRAS, 377, 1043
McQuinn M., Oh S. P., Faucher-Giguère C.-A., 2011, ApJ, 743, 82
Madau P., Meiksin A., Rees M. J., 1997, ApJ, 475, 429
Madau P., Rees M. J., Volonteri M., Haardt F., Oh S. P., 2004, ApJ, 604, 484
Mellema G. et al., 2013, Exp. Astron., 36, 235
Mesinger A., Furlanetto S., 2007, ApJ, 669, 663
Mesinger A., Bryan G. L., Haiman Z., 2006, ApJ, 648, 835
Mesinger A., Furlanetto S., Cen R., 2011, MNRAS, 411, 955
Mesinger A., McQuinn M., Spergel D. N., 2012, MNRAS, 422, 1403
Mesinger A., Ferrara A., Spiegel D. S., 2013, MNRAS, 431, 621
Mesinger A., Greig B., Sobacchi E., 2016, MNRAS, 459, 2342
Mineo S., Gilfanov M., Sunyaev R., 2012a, MNRAS, 419, 2095
Mineo S., Gilfanov M., Sunyaev R., 2012b, MNRAS, 426, 1870
Mirabel I. F., Dijkstra M., Laurent P., Loeb A., Pritchard J. R., 2011, A&A, 528, A149
Morales M. F., 2005, ApJ, 619, 678
Morales M. F., Wyithe J. S. B., 2010, ARA&A, 48, 127
Morales M. F., Hazelton B., Sullivan I., Beardsley A., 2012, ApJ, 752, 137
Oh S. P., 2001, ApJ, 553, 499
Paardekooper J.-P., Khochfar S., Dalla Vecchia C., 2015, MNRAS, 451, 2544
Pacucci F., Mesinger A., Mineo S., Ferrara A., 2014, MNRAS, 443, 678
Parsons A. R. et al., 2010, AJ, 139, 1468
Parsons A., Pober J., McQuinn M., Jacobs D., Aguirre J., 2012a, ApJ, 753, 81
Parsons A. R., Pober J. C., Aguirre J. E., Carilli C. L., Jacobs D. C., Moore D. F., 2012b, ApJ, 756, 165
Parsons A. R. et al., 2014, ApJ, 788, 106
Patra N., Subrahmanyan R., Sethi S., Shankar N. U., Raghunathan A., 2015, ApJ, 801, 138
Planck Collaboration XIII, 2016, A&A, 594, A13
Planck Collaboration XLVII, 2016, A&A, 596, A108
Pober J. C. et al., 2013, AJ, 145, 65
Pober J. C. et al., 2014, ApJ, 782, 66
Pober J. C. et al., 2015, ApJ, 809, 62
Pober J. C. et al., 2016, ApJ, 819, 8
Power C., Wynn G. A., Combet C., Wilkinson M. I., 2009, MNRAS, 395, 1146
Power C., James G., Combet C., Wynn G., 2013, ApJ, 764, 76
Press W. H., Schechter P., 1974, ApJ, 187, 425
Pritchard J. R., Furlanetto S. R., 2007, MNRAS, 376, 1680
Pritchard J. R., Loeb A., 2012, Rep. Prog. Phys., 75, 086901
Ricotti M., Ostriker J. P., 2004, MNRAS, 350, 539
Ricotti M., Gnedin N. Y., Shull J. M., 2001, ApJ, 560, 580
Santos M. G., Ferramacho L., Silva M. B., Amblard A., Cooray A., 2010, MNRAS, 406, 2421
Shaver P. A., Windhorst R. A., Madau P., de Bruyn A. G., 1999, A&A, 345, 380
Sheth R. K., Tormen G., 1999, MNRAS, 308, 119
Shimabukuro H., Semelin B., 2017, MNRAS, 468, 3869
Sobacchi E., Mesinger A., 2014, MNRAS, 440, 1662
Sokolowski M. et al., 2015, PASA, 32, e004
Sun G., Furlanetto S. R., 2016, MNRAS, 460, 417
Tegmark M., Silk J., Rees M. J., Blanchard A., Abel T., Palla F., 1997, ApJ, 474, 1
Thompson A. R., Moran J. M., Swenson G. W., 2001, in Interferometry and Synthesis in Radio Astronomy, 2nd edn. Wiley, New York
Thyagarajan N. et al., 2013, ApJ, 776, 6
Thyagarajan N. et al., 2015a, ApJ, 804, 14
Thyagarajan N. et al., 2015b, ApJ, 807, L28
Tingay S. J. et al., 2013, PASA, 30, 7
Tozzi P., Madau P., Meiksin A., Rees M. J., 2000, ApJ, 528, 597
Trott C. M., Wayth R. B., Tingay S. J., 2012, ApJ, 757, 101
Tzanavaris P., Georgantopoulos I., 2008, A&A, 480, 663
van Haarlem M. P. et al., 2013, A&A, 556, 2
Vedantham H., Shankar N. U., Subrahmanyan R., 2012, ApJ, 745, 176
Voytek T. C., Natarajan A., García J. M. J., Peterson J. B., López-Cruz O., 2014, ApJ, 782, L9
Watkinson C. A., Pritchard J. R., 2015, MNRAS, 454, 1416
Wouthuysen S. A., 1952, AJ, 57, 31
Xu H., Ahn K., Wise J. H., Norman M. L., O'Shea B. W., 2014, ApJ, 791, 110
Xu H., Wise J. H., Norman M. L., Ahn K., O'Shea B. W., 2016, ApJ, 833, 84
Yatawatta S. et al., 2013, A&A, 550, A136
Yue B., Ferrara A., Salvaterra R., Xu Y., Chen X., 2013, MNRAS, 433, 1556
Zahn O., Mesinger A., McQuinn M., Trac H., Cen R., Hernquist L. E., 2011, MNRAS, 414, 727
Zaroubi S., 2013, in Wiklind T., Mobasher B., Bromm V., eds, Astrophysics and Space Science Library, Vol. 396, The First Galaxies. Springer-Verlag, Berlin, p. 45
Zel'dovich Y. B., 1970, A&A, 5, 84

APPENDIX A: SENSITIVITY CURVES

In Figs A1 and A2, we present the mock 21 cm PS (black curves) for both of our EoR source models FAINT GALAXIES and BRIGHT GALAXIES, respectively. We show the 21 cm PS for each of the eight co-evolution redshifts we use in this work to achieve our astrophysical constraints, covering both the EoR and the EoH. For each, we provide the corresponding total noise PS for HERA (blue) and SKA (red) for our assumed 1000 h observational strategy (see Section 2.3 for more details). Finally, the black dashed curve is the 20 per cent modelling uncertainty, which we have applied to the mock 21 cm PS (it is applied to the sampled 21 cm PS not the mock observation in 21CMMC) to provide reference to the dominate source of error at any k-mode.

It is interesting to note that while most of the EoH parameters are tightly constrained for both mock observations, these constraints appear to arise solely from a relatively narrow range in redshifts, which pick up the rise and fall of the large-scale power. This emphasizes the importance of observing the cosmic 21 cm signal in an extended frequency range, allowing us to pick up the major milestones in the signal which drive strong astrophysical parameter constraints.

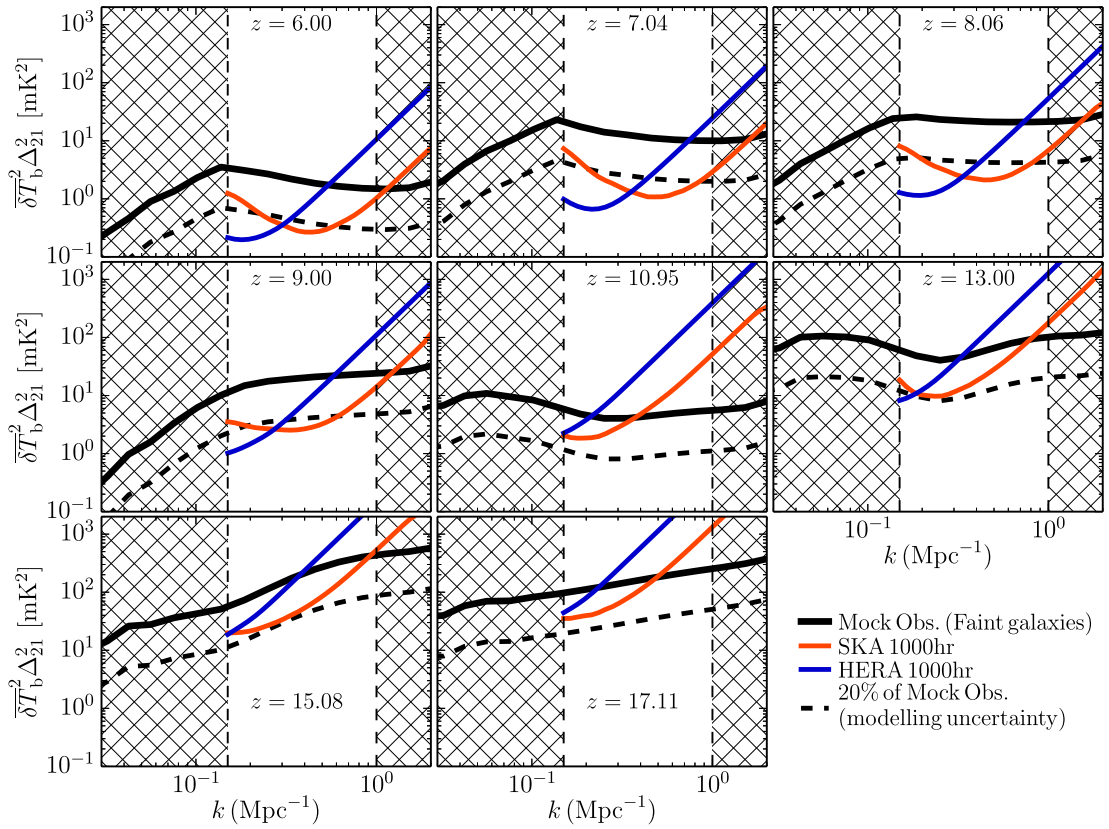

Figure A1. The 21 cm PS (black, solid curve) of the FAINT GALAXIES (Section 3) mock observation at all eight co-eval redshifts used in this work. Red and blue solid curves correspond to the noise curves (thermal + sample variance) for an assumed 1000 h observation with the SKA and HERA, respectively (see Section 2.3). The black dashed curve is 20 per cent of the mock 21 cm PS, highlighting the scale of the assumed modelling uncertainty used in this work. Representing it in this format highlights the dominant source of error at any redshift, or k-mode. Hatched regions correspond to k-modes beyond the 21 cm PS fitting region used in 21CMMC.

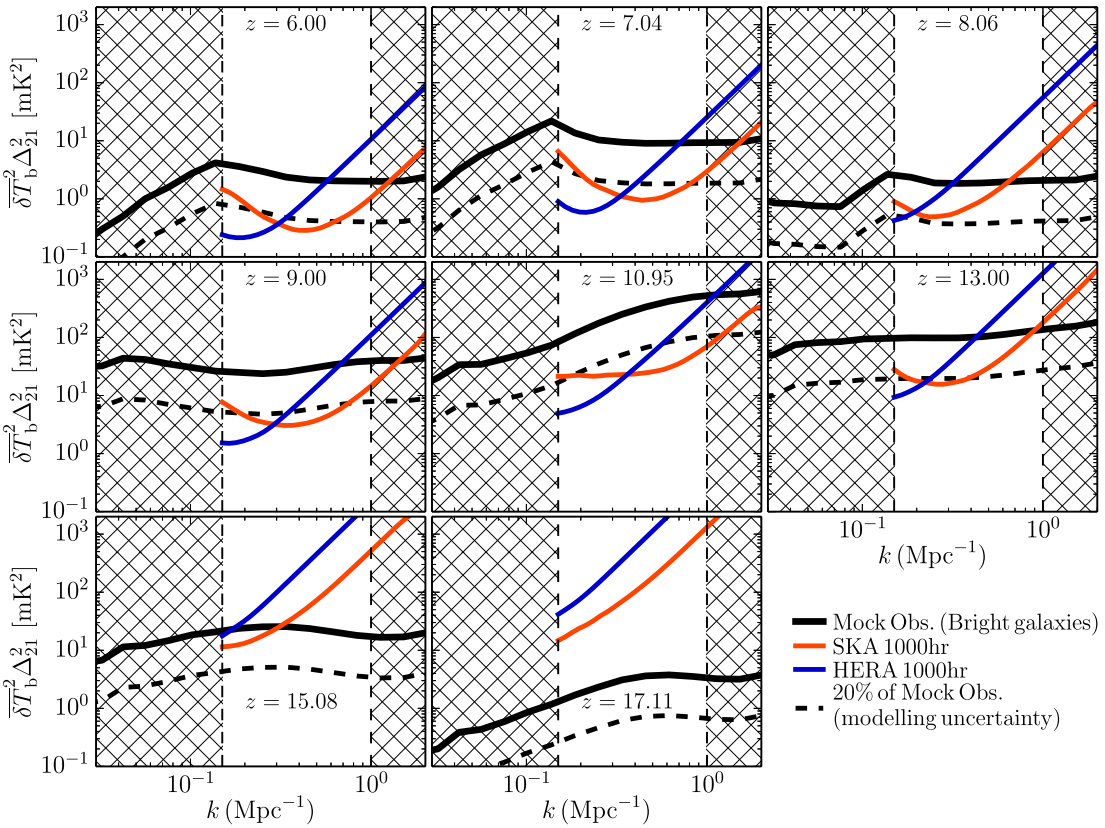

Figure A2. Same as Fig. A1 except now for the BRIGHT GALAXIES model (see Section 3).

This paper has been typeset from a TEX/LATEX file prepared by the author.